ANL/NE-13/16

Dry Cask Storage Inspection and Monitoring

Interim Report
September 2012

Nuclear Engineering Division
Argonne National Laboratory

ANL/NE-13/16

Dry Cask Storage Inspection and Monitoring

Interim Report
September 2012

prepared by:

Sasan Bakhtiari[1]
Thomas W. Elmer[1]
Eugene Koehl[1]
Ke Wang[1]
Apostolos C. Raptis[1]
Dennis C. Kunerth[2]
Sandra M. Birk[2]

[1]Nuclear Engineering Division, Argonne National Laboratory
[2]Nuclear Materials Disposition and Engineering, Idaho National Laboratory

Prepared for the
U.S. Department of Energy
Office of Nuclear Energy
Under DOE Idaho Operations Office
Contract DE-AC07-05ID14517

Contents

List of Figures

1. Introduction

Recently, the U.S. Nuclear Regulatory Commission (NRC) issued the guidance on the aging management of dry storage facilities that indicates the necessity to monitor the conditions of dry cask storage systems (DCSSs) over extended periods of time.[1] Part of the justification of the aging management plans is the requirement for inspection and monitoring to verify whether continued monitoring, inspection or mitigation are necessary. To meet this challenge Argonne National Laboratory (ANL) in collaboration with Idaho National Laboratory (INL) is conducting scoping studies on current and emerging nondestructive evaluation/examination (NDE) and online monitoring (OLM) technologies for DCSS integrity assessments. The scope of work plan includes identification and verification of technologies for long-term online monitoring of DCSSs' crucial physical parameters such as temperature, pressure, leakage and structural integrity in general. Modifications have been made to the current technologies to accommodate field inspections and monitoring. A summary of the scoping studies and experimental efforts conducted to date as well as plans for future activities is provided below.

2. Scoping Studies and Summary of Activities

The overall objective of the first phase of this project was to perform a scoping study to identify those sensors and techniques that have the most promising commercial viability and fill a critical inspection or monitoring need. Candidates considered include sensors to monitor real-time material degradation and in-situ nondestructive evaluation/inspection (NDE/NDI) of dry cask storage systems (DCSSs). Some background information and a summary of scoping studies performed at ANL leading to identification of a number of candidate technologies are presented next.

Starting in 1985, dry cask storage systems (DCSSs) for spent nuclear fuel (SNF) have been in use to meet the shortage of wet storage facilities. A DCSS keeps the long cooled SNF dry and stores it in an inert atmosphere. The systems come in various designs of metal and concrete casks intended for on-site storage. By the end of 2010, the total U.S. inventory of SNF was 65,200 metric tones of uranium.[2] About one quarter of the SNF is stored in DCSS and this ratio will only increase with time.

A variety of DCSS designs have been developed by the industry and licensed by the NRC since the mid 1980's. Designs of DCSS are divided into two major types: those with welded metal canisters of SNF, and those with bolted metal casks of SNF. By the end of 2010, there are 1495 DCSSs in use.[3,4,5] Of these, 1321 units (88%) are welded canisters and 174 units (12%) are bolted casks.

With the recent cancellation of the Yucca Mountain repository and no clear path forward for SNF disposition emerging from the draft report of the Presidential Blue Ribbon Committee on America's

[1] "Standard Review Plan for Renewal of Spent Fuel Dry Cask Storage System Licenses and Certificates of Compliance," U.S. NRC NUREG-1927, March 2011.
[2] Used Nuclear Fuel Storage Maps, Nuclear Energy Institute (2011), http://www.nei.org/resourcesandstats/documentlibrary/nuclearwastedisposal/graphicsandcharts/used-nuclear-fuel-storage-map.
[3] Dry Cask Storage in the U.S. by Vendor, StoreFUEL, 11-127 (March 3, 2009).
[4] Dry Cask Storage in the U.S. by Vendor, StoreFUEL, 12-140 (April 6, 2010).
[5] Dry Cask Storage in the U.S. by Vendor, StoreFUEL, 12-158 (October 4, 2011).

Nuclear Future,[6] potentially much longer times (100-300 years) of dry-cask storage must now be envisioned for SNF before final disposition. Mechanisms for degradation of DCSSs that are too weak (or inoperative) in the short term may become important to the safety functions of the system, structure or components (SSCs) over such prolonged periods. For example, the possibility of excessive dry out of concrete overpacks in a desert climate, corrosion of concrete rebar in a marine climate, or stress corrosion cracking (SCC) of welds on storage canisters need to be considered, and, if possible, monitored.

Video and visual/photographic inspections of the cask exterior and interior surfaces are among the most prominent NDE/NDI methods employed during periodic inspections. In general, the entire cask exterior is video examined, supplemented by direct visual inspection, for evidence of degradation and deterioration (cracks, pitting, corrosion, thread damage). Due to limitations associated with accessibility to the canisters, miniature cameras are typically used for this purpose.

In addition to visual inspections, radiation surveys and confinement/pressure monitoring, temperatures are measured in all DCSSs employing concrete over-packs or storage modules. These systems have air inlet ports at the bottom of the module and exhaust ports at the top. This permits natural convection cooling of the cask or canister. At a minimum the exhaust air temperature at the top of the cask/module is monitored. Significant increase in this temperature indicates overheating of the storage cask/canister. The air inlet and outlet ports are also inspected daily for blockages and remedial action taken when necessary. In DCSSs using concrete modules to house canisters of SNF, e.g., NUHOMS, the temperatures of the metal heat shields protecting the interior concrete surfaces are also monitored. Again this can indirectly indicate canister overheating.

The functionality and effectiveness of components that provide radiation shielding, as well as those related to overall structural integrity (neutron shielding, overpacks/ storage modules, and concrete pads), are ensured by periodic visual inspections and/or measurements taken with portable equipment/instrumentation. If necessary, remedial action can then be taken. Continuous monitoring is, in general, only applied to components and structures that are directly related to confinement. Monitoring the pressure of the dry storage canisters/casks is one approach to detecting the loss of confinement.

NRC regulations require that DCSSs must have the capability for continuous monitoring on temperature, pressure, structure stability, leakage and degradation in order to determine when corrective action must be taken to maintain safe storage conditions. Methods and techniques that have been employed to monitor the conditions of DCSS during operation include:

1) Cladding temperature monitoring during drying: Currently inferred from measured water gap temperature and COBRA calculations, temperature-indicating radio frequency identification devices are proposed for near-term deployment.
2) SNF canister temperature monitoring: Currently inferred from thermocouple reading at surface and COBRA calculations, thermal imaging using borescope is proposed for near-term deployment.
3) SNF canister leakage identification: Currently no techniques are employed. Outer weld inspection using borescope is proposed for near-term deployment.

[6] Reactor and Fuel Cycle Technology Subcommittee Report to the Full Commission, Blue Ribbon Committee on America's Nuclear Future, Washington DC (June 2011).

4) Bolted cask leakage identification: Currently it is identified by monitoring the pressure change in space between inner and outer lids. The current method is sufficient.
5) Lack of air cooling: Currently it is monitored by daily inspection of DCSS cooling vents for debris. Temperature-indicating radio frequency identification (RFID) devices placed in vents are proposed for near-term deployment.
6) Concrete structural stability monitoring: Currently visual inspection of concrete surfaces for defects is employed. Programmed visual inspection, Schmidt Hammer, and γ imaging are proposed for near-term deployment.
7) SNF degradation/relocation: Currently no techniques are employed. Monitoring the changes in DCSS thermal image and γ imaging are proposed for near-term deployment.
8) Surface γ dose rate: Currently routine radiological surveillance of DCSSs is employed. A method that integrates the visual inspection and γ imaging is proposed for near-term deployment.

A number of existing and emerging OLM technologies including RFID, resistance temperature detector (RTD), ultrasonic temperature sensors, and speed of sound devices have been identified for monitoring of canister temperature, temperature gradient, cask or canister leakage and SNF degradation during normal operation of DCSSs. More detailed information on this subject is provided in the ANL report to the NRC entitled, "Extended In-Situ and Real Time Monitoring – Long-Term Dry Cask Storage of Spent Nuclear Fuel".[7]

The temperature of dry cask, both inside and outside the canister, is a critical parameter to monitor for the safe storage of spent fuel. When a leakage occurs, a local hot spot will be created near the leaking area. Also, the temperature distribution over the DCSS canister is a general indicator of the state of the spent fuel and the integrity of the components inside the vessel. In this work, ultrasonic and Johnson noise thermometry were selected for monitoring and profiling of the temperature over large areas of the canister, allowing more accurate detection and localization of potential leakages. A dry cask simulation test stand has been assembled at Argonne for experimental assessment of the proposed techniques. This small scale mock-up test facility allows continuous (24/7), unattended operation of a steel vessel wall section at temperatures of up to 300°C. The test stand allows ramping of the temperature of the vessel section up to 650°C with an operator in attendance for the purpose of aging the temperature sensors. A heating element, mounted inside the vessel, generates a temperature gradient that represents the scenario of dry cask leakage. An ultrasonic temperature probe, type N thermocouples (NTC), and resistance temperature detectors (RTD) are installed on the outside wall of the vessel to measure and profile the temperature. Long term monitoring of DCSSs requires employment of extremely rugged instrumentation that are preferably self-calibrating and are easily replaceable. To that end, the OLM sensor technologies being evaluated in this work were selected based on their potential to meet these stringent requirements.

In a collaborative effort between INL and ANL, promising in-situ NDE methods for periodic inspection of canisters are also being evaluated under this project. Eddy current testing (ECT) is a prominent electromagnetic NDE method for rapid detection and characterization of surface and sub-surface degradation/damage in metallic and other electrically conducting materials. Accessibility issues,

[7] J.D. Lambert, S. Bakhtiari, I. Bodnar, C. Kot, J. Pence, "Extended In-Situ and Real Time Monitoring – Long-Term Dry Cask Storage of Spent Nuclear Fuel," ANL/NE-12/18, under review by the U.S. Nuclear Regulatory Commission, March 2012.

however, limit the applicability of this technique to examination of dry storage canisters. An advanced ECT method based on array probe technology is being evaluated in this work for examination of both welded and bolted canister designs. Experimental efforts have thus far been focused on the evaluation of surface-conforming array probes for the more challenging problem of weld inspection. An array probe with driver-pickup elements is being evaluated for this purpose. A number of calibration standard samples available at INL are currently being used in these investigations. In parallel, theoretical simulations are being conducted to help optimize the probe design. This is done to increase the probe coverage while maintaining the sensitivity and spatial resolution for detection of limiting flaws. The optimized array probe design is expected to eliminate the need for continuous scanning of the probe in tight spaces. Finally, advanced signal processing and data analysis algorithms developed earlier at Argonne are being adapted to the processing of NDE data from DCSSs. Such tools are expected to help improve detection and characterization of potential flaws in DCSS components and to further help automate the inspection process.

3. Evaluation of In-Situ Inspection and Online Monitoring Technology

In addition to the scoping studies described above, work was also performed on assessing some promising inspection and monitoring techniques for long-term DCSS integrity assessments. Experimental efforts in this area are being conducted in parallel at ANL and at INL. Based on the results of scoping studies and past experience at ANL, four emerging sensor technologies were selected for OLM of canister temperature. It is worth noting that the term "emerging" technology here refers to any technique that has not yet gained widespread acceptance for routine field use by the NPP industry, even though the technique itself may have been originally developed and demonstrated in the past. A mock-up was assembled and fitted with contact type sensors and the associated instrumentation for evaluation of those techniques. Additionally, a novel non-contact technique for standoff monitoring of structures is currently being evaluated under this project. A millimeter-wave (mmW) radiometer developed earlier at Argonne is being adapted for in-situ imaging of temperature distribution of DCSSs. In parallel, efforts are also being made to improve current state-of-the-art in NDE of DCSS canisters. The selected technology for this purpose is eddy current testing with high-resolution array probes. A number of data sets collected at INL have been sent to ANL for further analysis. Advanced data analysis techniques developed previously at ANL are being used to improve detectability of potential flaws at welds. Numerical electromagnetic modeling is also being performed at ANL to optimize the array probe design. A brief description of the experimental investigations conducted to date is provided below.

3.1 Mock-up Test Facility for Assessing OLM Techniques

A mock-up test facility was established to help assess promising technologies for OLM and in-situ inspection of DCSS metal canisters. The Dry Cask Simulation Test Stand is a structural metal (Unistrut) frame with insulated, sheet metal walls. Figure 1(a) shows the test stand with protection covers in place, which prevent the operating personnel from contacting thermally hot surfaces and/or electrical hardware when the mockup is under test and being heated. The test stand with several covers removed is displayed in Fig. 1(b). As shown in that figure, the frame is divided into two sections: the top section houses a dry cask simulator, heating element, process thermocouples and calibrated temperature probes; the bottom section houses temperature and power control equipment.

(a)

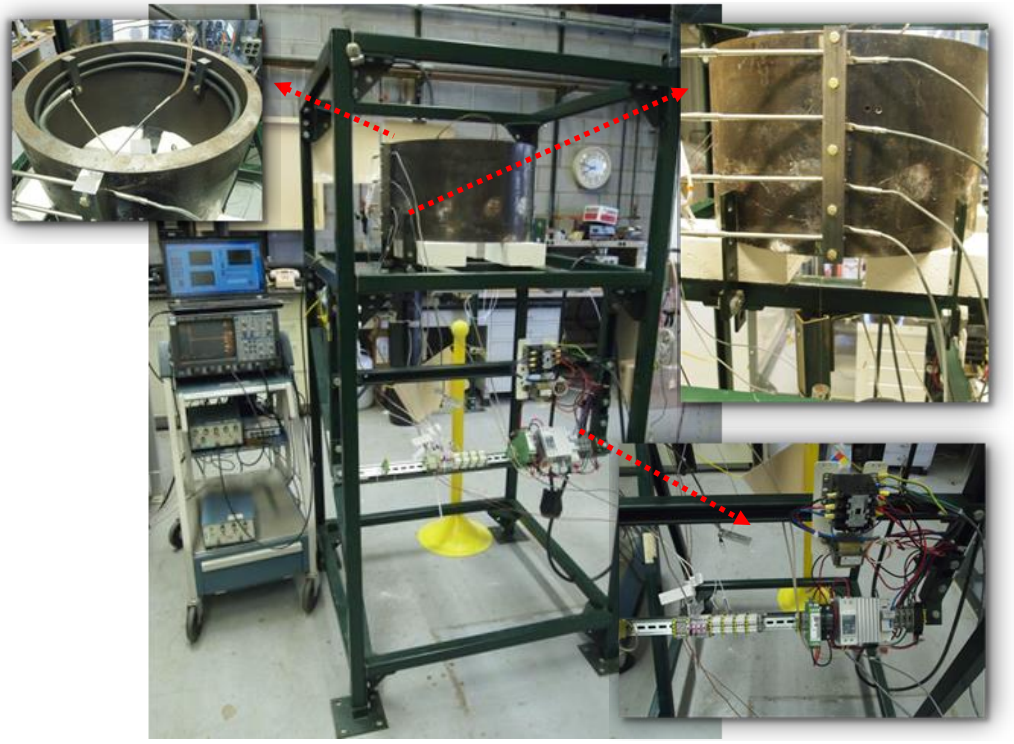

(b)

Fig. 1. Dry Cask Simulation Test Stand (a) with and (b) without protection cover. Also shown are enlarged pictures of different sections of the mock-up and instrumentation used for online monitoring.

The DCSS mockup is designed to operate at temperatures up to 650°C using a 7 kW heating element. Air flow dampers, heat shields and insulating materials allow gross control over convection and radiation heat losses. It is designed to conduct continuous (24/7), unattended operation with temperatures up to 300°C and temperature ramping up to 650°C with an operator in attendance to monitor the aging process and stability of the applied sensors.

As shown in Fig. 1(b), the canister mockup (CM) is comprised of an 11-inch long section of 18-inch diameter, mild-steel pipe with a 1-inch thick wall. It is isolated from the metal frame by furnace insulating blocks (fire brick) and oriented to promote an axial temperature differential.

The CM is instrumented with four NTCs paired with four, 100-ohm RTD probes arranged axially. Type-N TCs exhibit better stability than traditional type E, J, K and T, base-metal thermocouples. RTD probes serve a dual purpose by providing an immediate indication of temperature and a stable noise source for Johnson Noise measurement. The calibrations of the type-N thermocouples and RTDs are NIST traceable. The ultrasonic temperature probe (UTP) is mounted beside the NTCs and RTDs to compare their performance in parallel.

The heating element is a 105-inch long, ½-inch diameter Cal-rod wound to conform to the inner surface of the CM. It is located within the top 3-inches of the CM. Its operating temperature is monitored by a dual type-K thermocouple (KTC) inserted ~ ½-inch into the wall of CM. One of the KTC elements is connected to the input of a set-point temperature controller (PID). The second KTC element is connected to a high-temperature limiting, fail-safe (FS) controller. Accuracy of this TC pair is the greater of ±2.2°C or 0.75% of the displayed value.

Set-point temperature control is accomplished using Eurotherm 2000 series PID and limit controllers and a TE10 power control. Final set-point controller accuracy is the greater of ±1°C or 0.25% of the displayed value. The overall temperature accuracy is the sum of the KTC-controller combination or ±3.2°C or 1.00% of the displayed value.

The PID controller allows fine-tuning of the desired operating temperature and includes an optional timed dwell function. The FS control provides high-temperature cut-off in the event the PID is set to a wrong temperature or exceeds a preset high temperature or either KTC should fail due to short or open circuit conditions. The PID and TE10 power control provide heater failure detection and alarm. All control and signal voltages operate at or below 24 volts ac/dc, and power voltages operate at 240 Vac or less.

The test stand is subjected to a safety review which includes an electrical equipment inspection to ensure the operator is protected from elevated temperatures and potential electrical shock hazards.

3.1.1 Data Acquisition System

Temperature data is acquired using a National Instruments CompactDAQ system with an RTD module (NI-9217) and a Thermocouple module (NI-9211). Voltage data is currently acquired using a NI USB-4431 on loan to the project, which supports 24-bit, 100 kS/s data acquisition rate. In reference to Fig. 2, the DAQ systems are connected to a laptop through USB ports.

Data acquisition is performed in LabVIEW. The LabVIEW diagram is shown in Fig. 3. After initialization (light blue on the left), data acquisition from multiple sources as well as file writing are

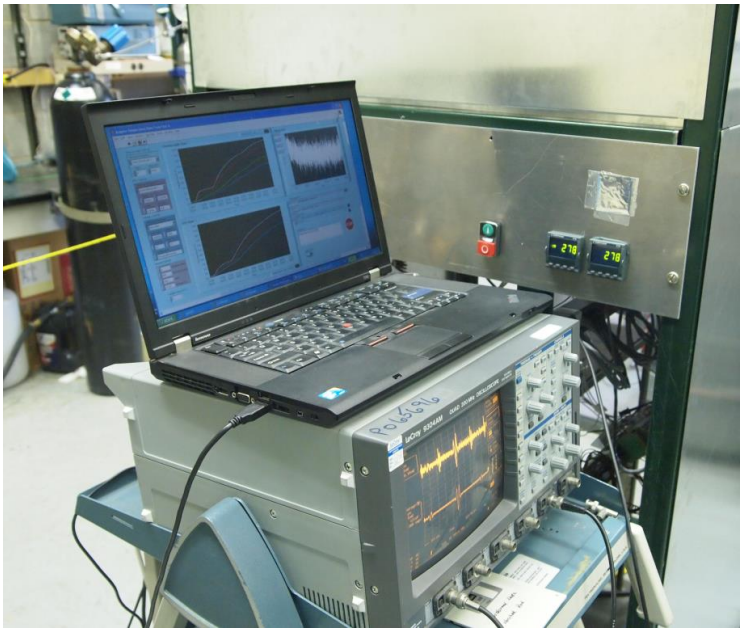

(a)

(b)

(c)

Fig. 2. Data collection hardware, consisting of: a) Laptop running LabVIEW to collect temperature data atop the oscilloscope displaying UTP data. b) NI CompactDAQ with Thermocouple (NI-9211) and RTD (NI-9217) modules. c) NI USB-4431 for voltage measurements

executed in separate loops (multithreaded), shown here with different colors. The Sub-VIs in each loop perform the actual acquisition. Using multithreading in the VI allows us to collect from all data sources simultaneously, while allowing the option to allow faster sources to sample more frequently than slower ones if desired. Overall timing is managed by a 'GO' notifier controlled by the green loop at the bottom. Data synchronization for saving to the strip chart file is managed by a rendezvous at which any, or all, of the acquisition loops can wait. Setting the master control interval to zero and rendezvousing with the fastest source allows us to acquire data as fast as our sources would allow. Similarly, rendezvousing with all sources enables the slowest source to synchronize acquisition. Raw data is passed to the binary file sub-VI via data queues, allowing the system to move on to the next data collection while saving in the background. An indicator on the front panel alerts the user if the data queue is building up too quickly. After all loops have been terminated, the rendezvous, notifiers, and queues are released and an error message is displayed if necessary. The VI front panel is shown in Fig. 4(a).

Data is saved in two file formats. Summary data, such as temperature, RMS voltage, etc, are stored in a LabVIEW Measurement (LVM) ASCII file. This file can be read easily by Excel or MATLAB. However, the resolution of this data is limited to 6 significant figures. More accurate data is saved to a binary Technical Data Management Streaming (TDMS) file. This file stores complete voltage waveforms for calculating Johnson Noise, as well as the full resolution data from the temperature probes. In reference to Fig. 4(b), this data can be easily browsed in LabVIEW or imported to MATLAB via a number of import libraries available on Mathworks Central. Please check the glossary for the terms.

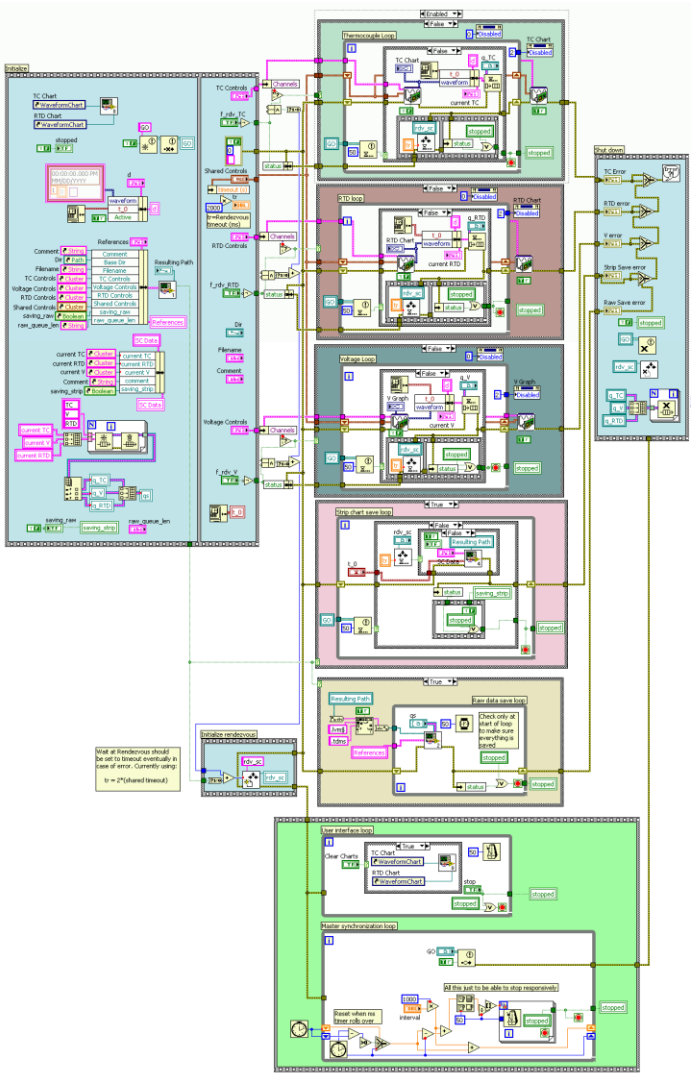

Fig. 3. LabVIEW diagram for the data acquisition VI.

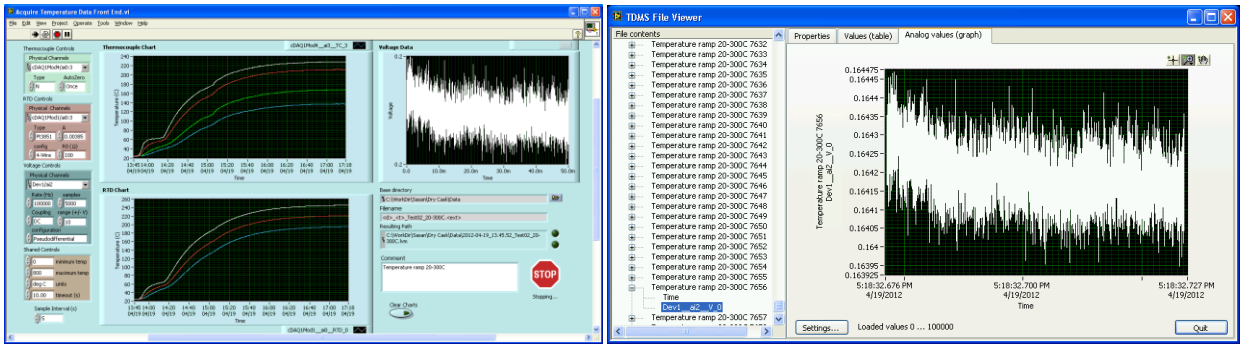

(a) (b)

Fig. 4. (a) LabVIEW data acquisition front panel and (b) TDMS file browser in LabVIEW.

3.1.2 Johnson Noise Thermometry (JNT)

Johnson Noise Thermometry (JNT) is a first-principles representation of temperature. It is immune from chemical and mechanical changes in the material properties of the sensor. It is based on the Nyquist equation that describes the voltage produced by the vibration of the electrons within a resistor at a given temperature.[8,9]

For frequencies below a few gigahertz, the Nyquist equation shows the relationship between the absolute temperature of a resistor (T), its resistance (R), the frequency band of measurement (Δf) and the measured mean-square noise voltage (V^2).

$$V^2 = 4k_B TR\Delta f \qquad (1)$$

where k_B represents Boltzmann's constant (1.38×10^{-23} Joules/Kelvin).

The main challenge for JNT is that it requires accurate, low-noise correlation techniques to measure the extremely small noise voltage (~1.2 nV/Hz$^{1/2}$) of a typical 100 Ω resistor at the triple point of water (T_{tpw} =273.16ºK).

The technique is used to monitor the electronic noise generated by a stable, 100 Ω platinum resistance thermometer (RTD). The RTD is excited by a stable, 1 mA dc current (at < 50 Vdc) and the resultant voltage (microvolts) is related to the International Temperature Scale of 1990. Signals used in noise thermometry are very small: a 100 Ω RTD at 300ºK and a frequency bandwidth of 100 kHz generates a noise signal of ~0.4 μ V_{rms}; the voltage across the RTD is 107.79 mV.

A schematic illustration of the measurement process is shown in Fig. 5. The mockup system provides the root mean square (RMS) and standard deviation (STD) of noise voltage, while the resistance of RTD is independently measured. The frequency band of measurement (Δf) is obtained by calibrating the measurement using a known temperature.

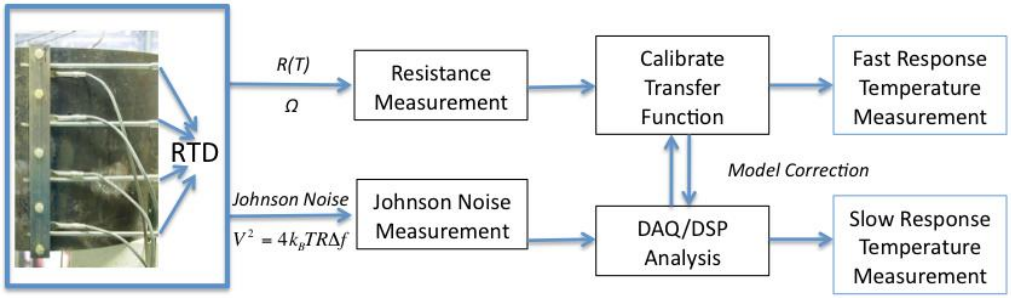

Fig. 5. Schematic drawing of JNT measurement.

[8] David E. Holcomb, Roger A. Kisner and Michael J. Roberts, " Johnson Noise Thermometry For Space Reactor Temperature Measurement", AIP Conf. Proc. 699, 567 (2004); doi: 10.1063/1.1649617

[9] Samuel P. Benz, Jifeng Qu, Horst Rogalla, D. Rod White, Paul D. Dresselhaus, Weston L. Tew and Sae Woo Nam, " Improvements in the NIST Johnson Noise Thermometry System," IEEE Transactions On Instrumentation and Measurement, Vol. 58, No. 4, April 2009.

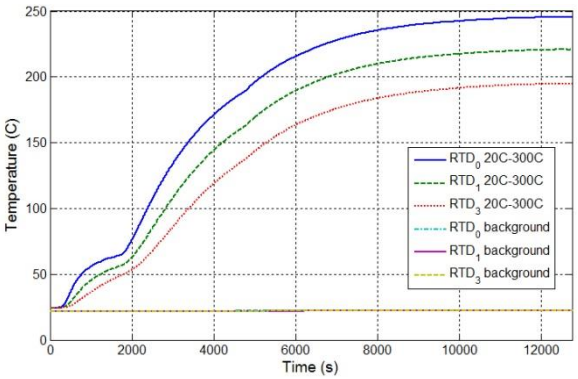

(a)

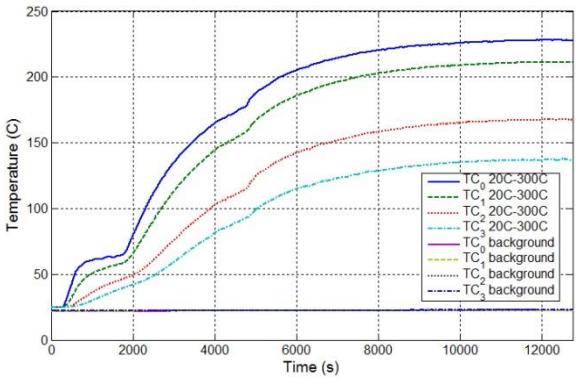

(b)

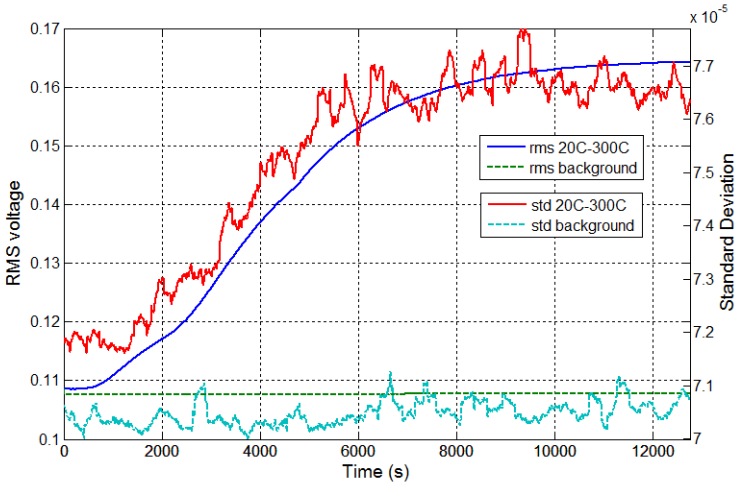

(c)

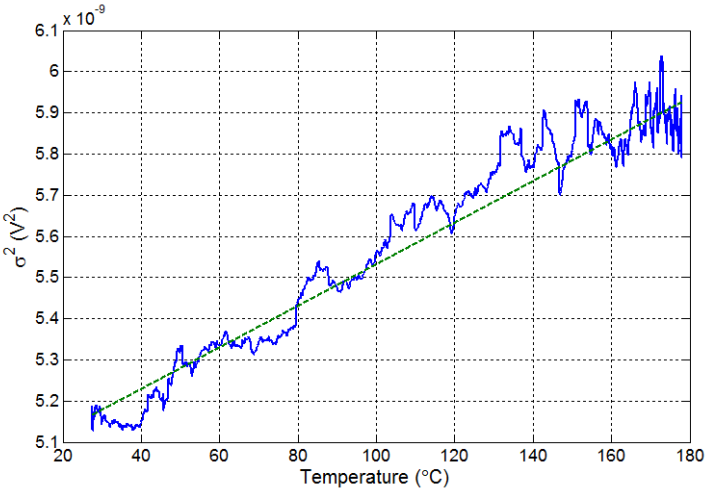

(d)

Fig. 6. Data collected as the mockup heated from 20°C to 300°C. a) RTD data, b) Thermocouple data, c) voltage-derived plots showing RMS value and standard deviation (a measure of noise), and d) the mean square of noise voltage level vs. temperature.

Results of initial testing are shown in Fig. 6. Data was collected while the mockup was heated from 20°C to 300°C. The measurements from RTDs and TCs are provided in Figs. 6(a) and 6(b), respectively. Both RTDs and TCs indicate the same trend with rising temperature. A close look of the results suggests that the difference in temperature reading of the same pair of RTD and TC is smaller at lower temperature (<150 °C) than that at higher temperature, which could provide important information on comparison of the stability of RTD/TC at elevated temperature. In addition, the measurements on the RMS value of the RTD voltage and the STD value of noise voltage at room temperature (as reference) and elevated temperature are given in Fig. 6(c). Figure 6(d) shows the relationship between mean square the noise voltage and temperature. The least square fit clearly indicates that the mean square of noise voltage level is a linear function of temperature, which matches well with the Nyquist equation.

3.1.3 Ultrasonic Temperature Probe (UTP)

The temperature gradient of a dry cask, both inside and outside the structure, is a critical parameter to monitor for the safe storage of spent fuel. The temperature and pressure inside the DCSS canister is always higher than that of the outside. When a breach in the shielding structure occurs, a local hotspot will be created around the leakage zone. The presence of high temperatures (to 1000 °C), high radiation fields, confined space, lack of visual access, and required resolution preclude the use of other temperature profiling techniques such as those based on fiber optic technology. The proposed UTP technique is a method of temperature measurement based on the principle that the acoustic velocity in all materials is a function of temperature. The sensor has a simple and rugged design that can sustain hostile environments encountered during long-term monitoring of DCSSs. Also, its flexible probe is capable of conforming to complex geometries, which is particularly suited to measurements where access is limited.

A pulse echo method is utilized in the UTP. By sending an ultrasonic pulse through a probe of known length, and measuring the time between the initial pulse and the reflection of the pulse from the opposite end of the probe, the average acoustic velocity (correspondingly, the average temperature of the probe), can be calculated. With more acoustic discontinuities, such as notches and sharp bends, the probe becomes a multipoint temperature sensor, where the average temperature of each segment is derived from the time of flight (TOF) of successive reflections.

A close look at the TOF expression of the echoes reveals the factors that determine the shift. The TOF of each echo has a simple expression:

$$t = \frac{2l}{V} \tag{2}$$

where l is the travel distance of the signal and V is the sound velocity in the waveguide. Then the difference of TOF under difference temperatures can be written as:

$$\delta t = \frac{2\delta l}{V_0^2} - t_0 \cdot \frac{\delta V}{V_0} \tag{3}$$

where

$$\begin{aligned} &\delta t = t_{T_0} - t_T;\ \delta l = l_0 \alpha (T_0 - T) \\ &t_0 = \frac{2l_0}{V_0};\ \delta V = V_0 - V_T \\ &V_0 = V(T_0);\ V_T = V(T) \end{aligned} \tag{4}$$

In which, α is the linear thermal expansion coefficient of the waveguide. For the chosen alloy, its α is a constant and *V(T)* is linearly decreasing within the tested temperature regime. Consequently, δt at the bending point and the end tip can be accurately measured. A linear relationship between δt and T is expected.[10]

The UTP has several advantages over other sensors. The most appealing characteristic of UTP is the ability to make temperature measurements at several positions along the probe, measuring the temperature profile, using a single sensor. It also has a compact design while maintaining a high durability under hostile environments. As no electrical insulation is required, shunting effects found in thermocouples and resistance temperature devices (RTDs) are eliminated. Furthermore, no clear line of sight is required, as is the case for most optical pyrometry applications.

UTP Design

Three types of UTP have been designed for different applications. They are straight UTP, notched UTP, and bent UTP, as shown in Fig. 7. The straight UTP has the capability to measure the temperature at a single location or provides the average temperature of the probe.

The UTP, shown in Fig. 7, consists of a magnetostrictive transducer and a thin magnetostrictive metal probe sectored by notches. The probe, 0.635 mm in diameter, is a cobalt/iron magnetostrictive alloy. The magnetostrictive transducer is a simple electrical coil that generates a magnetic field causing

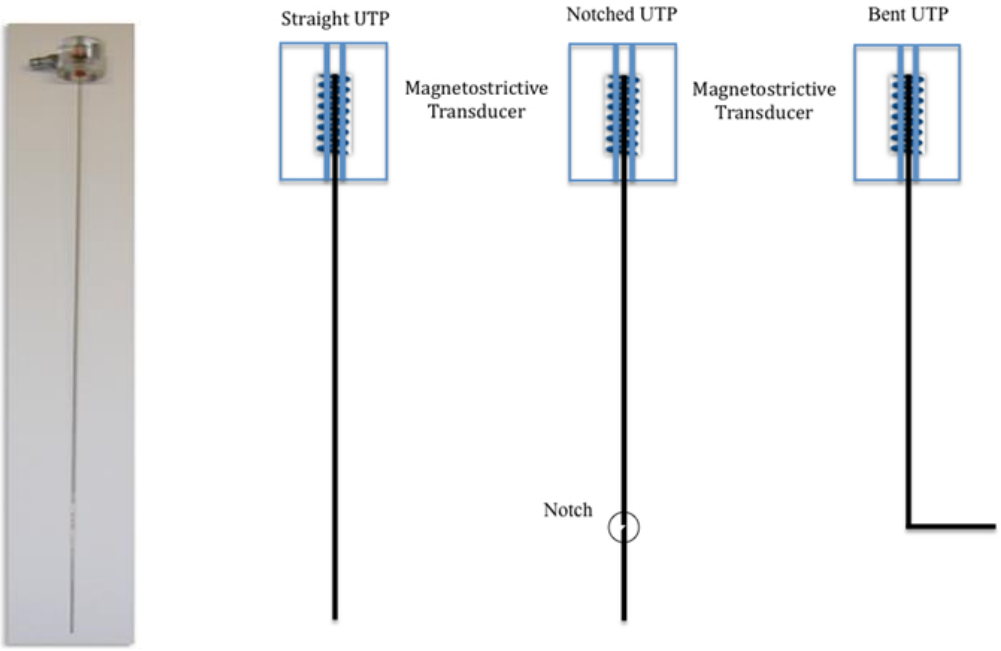

Fig. 7. Ultrasonic temperature probe developed at ANL and three alternative designs of UTP.

[10] K. Wang, H. T. Chien, S. Liao, L. P. Yuan, S. H. Sheen, S. Bakhtiari, and A. C. Raptis, "Ultrasonic and Electromagnetic Sensors for Downhole Reservoir Characterization," 36th Stanford Geothermal Program, SGP-TR-191, pp. 1039, 2011

the magnetostrictive probe to contract or elongate. In operation, the coil is energized with 200 kHz pulses to generate longitudinal waves of ~ 2.6 cm in wavelength propagating down the probe. As the wavelength is much longer than the probe diameter, these cylindrically guided longitudinal waves behave like surface waves (Lamb waves) with minimal attenuation. The reflected pulse train is established in the probe, from which the wave attenuation can be estimated. The estimated value is ~1.9 dB/m, which provides enough energy to effectively profile and monitor the temperature of DCSS. To measure the temperature profile along the probe, the probe is normally segmented into sections by bending the probe or cutting notches. In addition, the signal attenuation through the probe is negligible, when the bending angle of the probe is less than 80°, which makes it the ideal technique to monitor the temperature gradient around the circumference of DCSS. The surface disruption caused by a sharp bend or by a notch will result in reflection of a portion of the Lamb wave. As a result, multiple reflections can be detected.

Preliminary Test of UTP on a DCSS Mockup

These three UTP designs have been tested on a DCSS mockup introduced in the previous section. The UTP setup is shown in Fig. 8(a) and (b), where the magnetostrictive transducer is below the test section (not shown in the figures).

First, a straight UTP with a length of 60 cm was tested up to 300 °C. The results are plotted in Fig. 9. A schematic drawing of the working principle of straight UTP is shown in Fig. 9(a). Continuous measurements were taken as temperature increasing and four data sets are plotted in Fig. 9(b) to demonstrate the signal shift at elevated temperature.

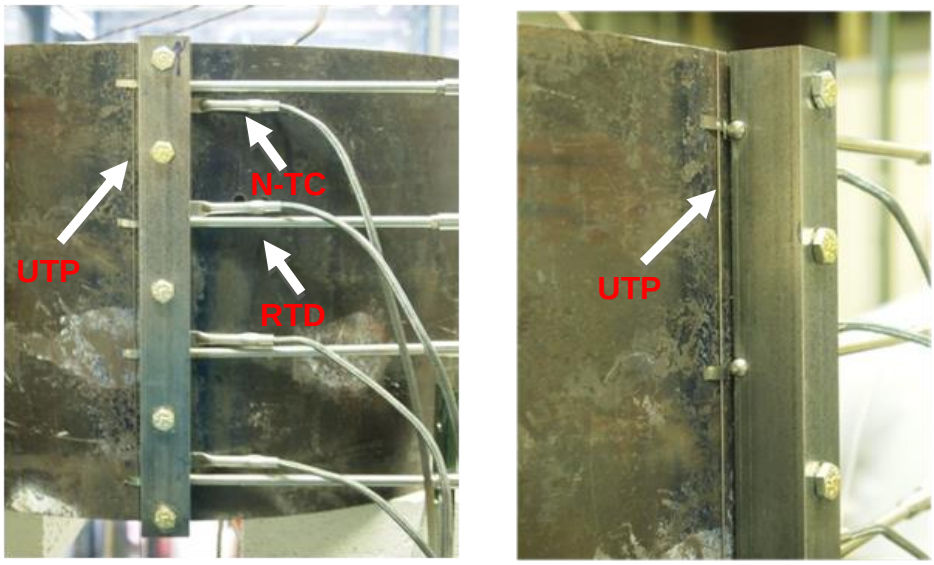

(a) (b)

Fig. 8. UTP mounted on the DCSS canister mockup.

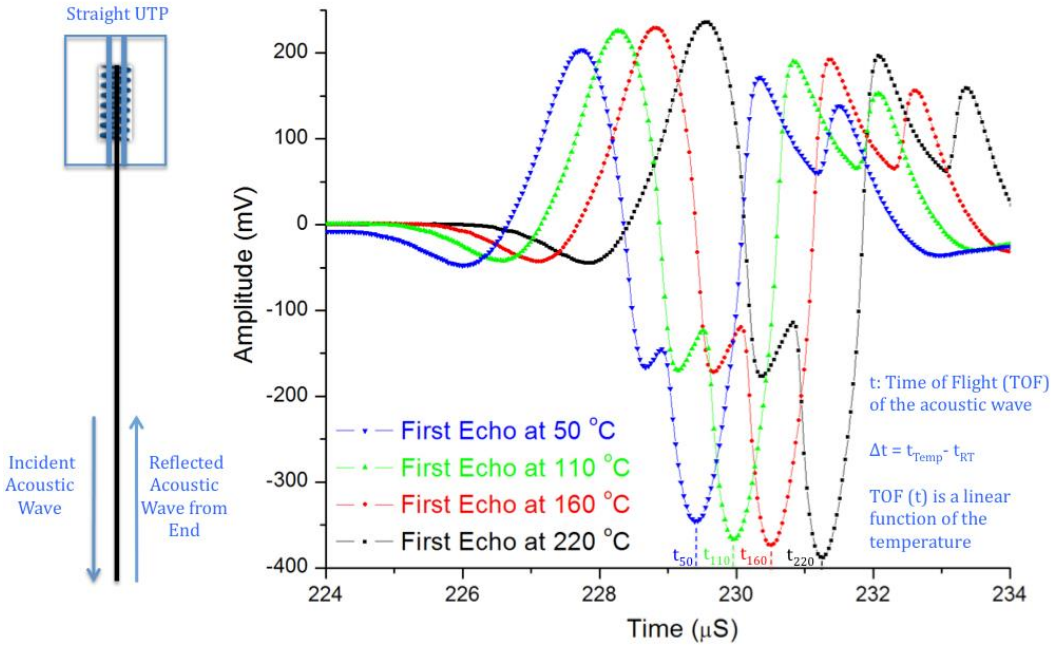

Fig. 9. Performance of straight UTP at elevated temperature.

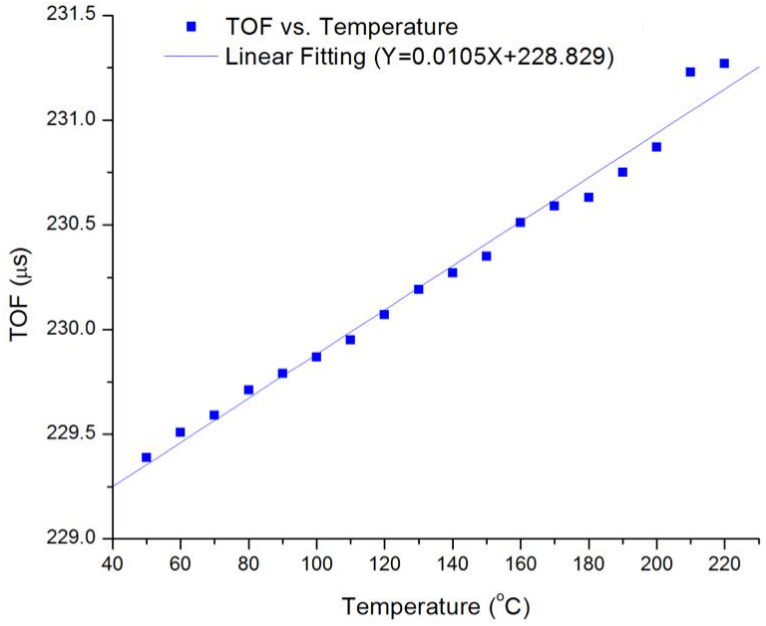

Fig. 10. The linear relationship between the measured TOF of straight UTP and the test temperature.

The linear relationship between the TOF and temperature increment is clearly proved in Fig. 10. With the established linearity, a continuous monitoring on temperature can be realized by TOF measurement.

A notched UTP, 60 cm in total length with a notch located 15 cm away from the end, was tested up to 245 °C. The results are plotted in Fig. 11. A schematic drawing of the working principle of a notched UTP is shown in Fig. 11(a). Different from the straight UTP, the extra discontinuity (notch) introduces additional reflections, as shown in Fig. 11. Continuous measurements taken with increasing temperature for four data sets are plotted in Fig. 11(b) to demonstrate the signal shift at elevated temperatures, which manifests its application to temperature profile measurement.

A bent UTP, 60 cm total length with a right angle bend at 15 cm away from the end, was tested up to 300 °C. The results are plotted in Fig. 12. A schematic drawing of the working principle of a bent UTP is shown in Fig. 12(a). Different from the straight UTP, the extra discontinuity (bending point) introduces additional reflections, as shown in Fig. 12. Continuous measurements were taken with increasing temperature for four data sets are plotted in Fig. 12(b) to demonstrate the signal shift at elevated temperature.

Both notched UTP and bent UTP play critical roles in monitoring the safe operation of DCSS. The notched UTP provides the average temperature of two consecutive notches, which enables temperature profiling with a single probe. The bent UTP has unique applications for DCSS with complex geometry. Even with a right angle, measurement of the TOF of bent section is still able to provide important temperature information. Efforts included 1) conducting further analysis of the linear relationship between the measured TOF from notches, bending point, or probe ends and the tested temperature; 2) constructing a probe with multiple notches for temperature profiling of the test section in the DCSS mockup. Representative data collected with the UTP sensor (see Fig. 8) is shown in Fig. 13. The TOF is plotted as a function of time (or alternatively temperature). The temporal data closely follows the trends measured using the RTD and TC sensors.

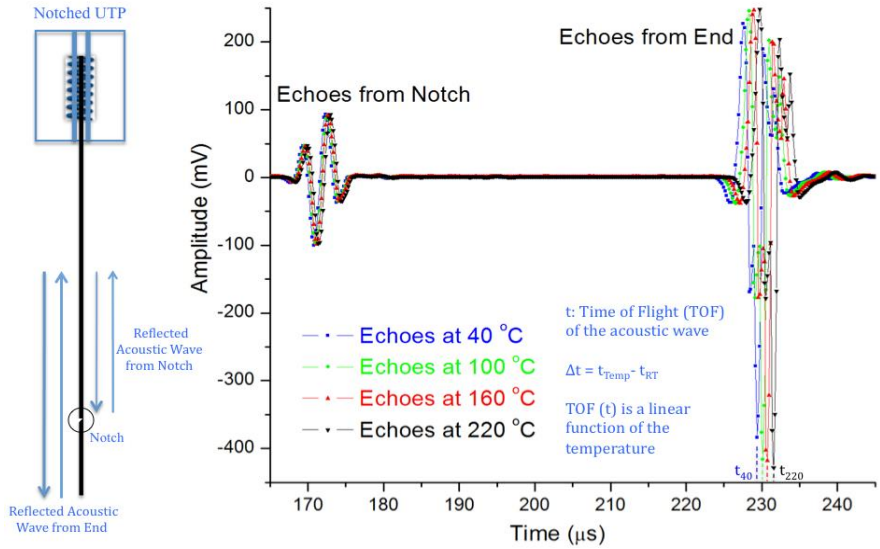

(a) (b)

Fig. 11. Performance of notched UTP at elevated temperature.

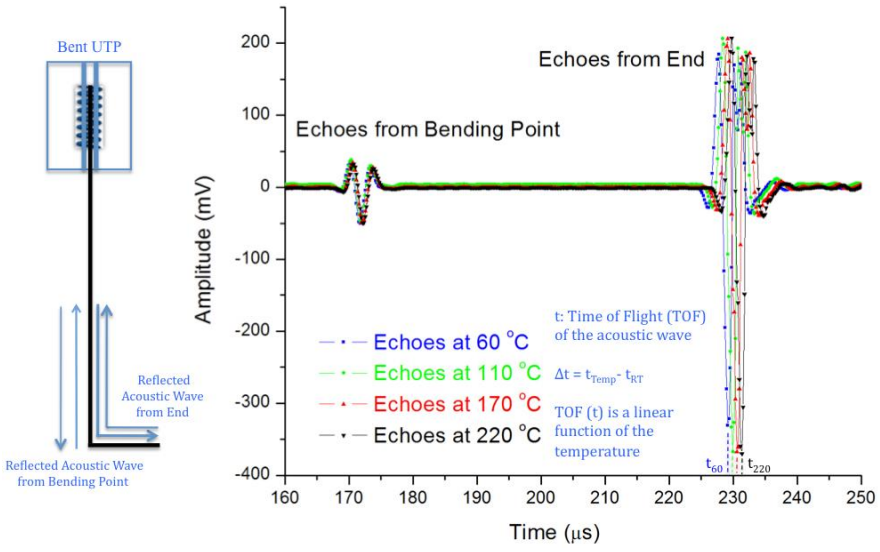

(a) (b)

Fig. 12. Performance of bent UTP at elevated temperatures.

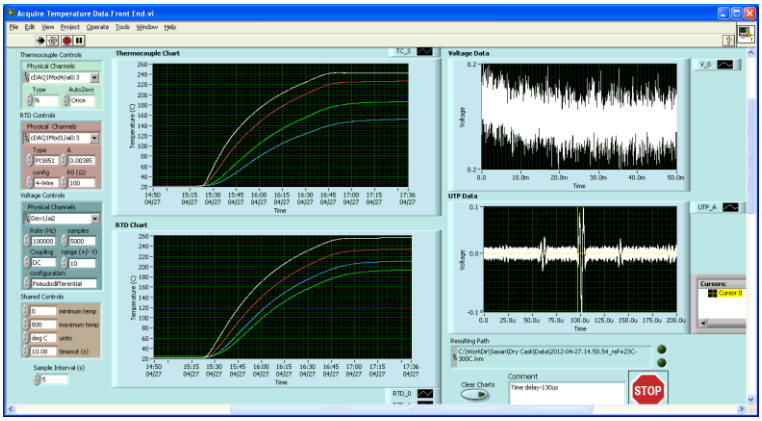

(a)

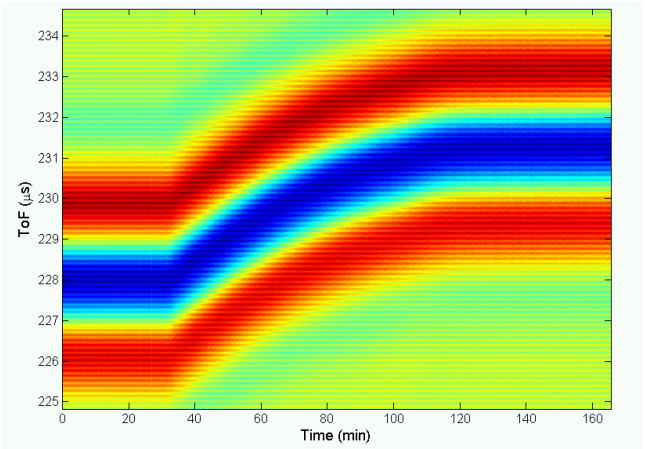

(b)

Fig. 13. (a) LabVIEW data acquisition front panel and (b) temporal data measured with the UTP.

3.1.4 Further Evaluation of UTP and JNT Sensors

Based on the results of initial investigations, experimental studies were conducted to further assess the performance of the two more promising techniques, namely, UTP and JNT, for long-term monitoring of DCSS temperature distribution. As noted earlier, the primary advantages of the UTP sensor include the robustness of the wireline probe for long-term monitoring under extreme conditions, the ability to obtain temperature profile with a single element, the surface conforming nature of flexible wireline probe allowing measurements over complex surfaces and in confined spaces, and adaptability to monitoring of existing DCSSs. The primary advantage of the JNT technique is its ability to provide calibration-free measurements through adaptation of conventional RTD probes for this purpose.

To further demonstrate the ability of the UTP sensor to provide temperature profile with a single probe, design modifications were made by including additional notches on the wireline probe. Figure 14 shows the approximate locations of the two notches on UTP. The first notch was placed at the same elevation as the second NTC/RTD set (from top). The second notch was placed at an elevation in between the third and the fourth NTC/RTD set. The measured ultrasonic echoes from specific locations including the end and the two notches are shown in Fig. 15. In the time of flight (ToF) results, the first echo is from the second notch, the second echo is from the first notch, and the third echo is the reflected signal from the end of the UTP. The intensities of echoes are mainly determined by the reflecting area at the measured locations. At the end of the UTP, all incident ultrasonic signals will be reflected back, therefore, the echo from end has the strongest intensity. Additional echoes observed in Fig. 15 after 250 μs are the result of multi-trip reflections along the wire. Higher order reflections that represent contribution of multiple echoes from different locations are not used here for temperature and temperature gradient measurements.

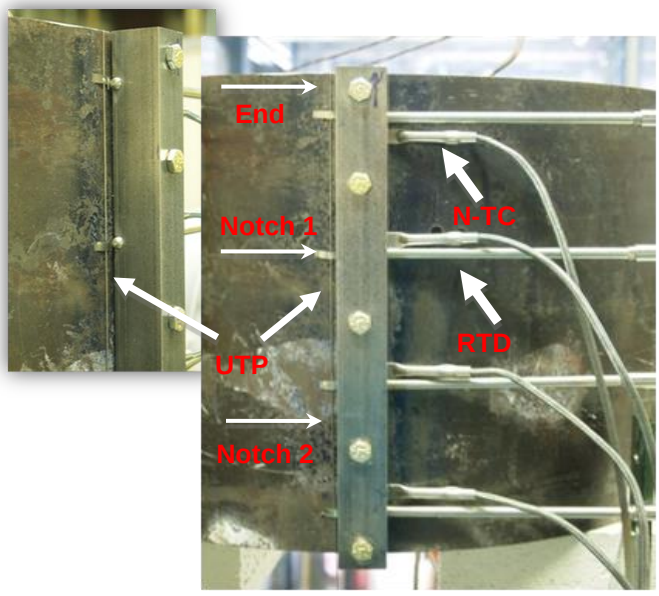

Fig. 14. The relative positions of notches on the UTP in straight conformation setup. The inset shows a clearer view of the UTP.

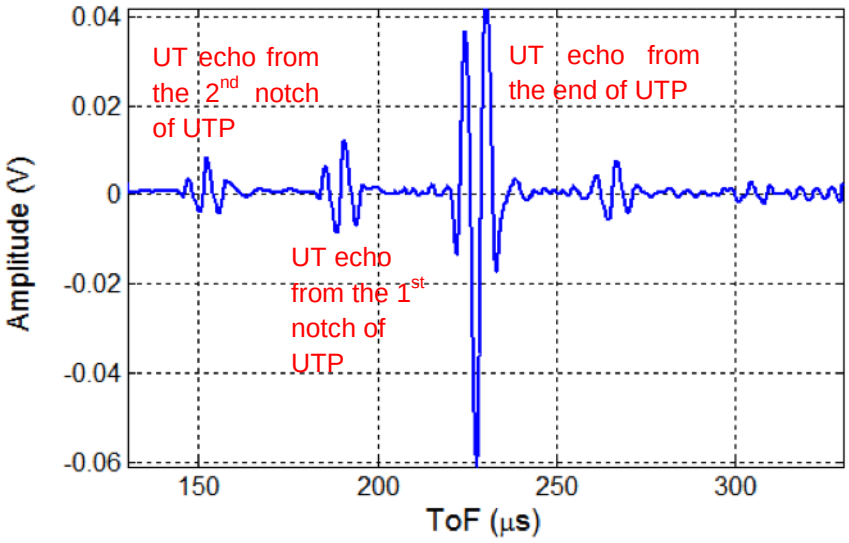

Fig. 15. Time-of-flight measurement of ultrasonic echoes from specific locations on UTP at 20°C.

Figures 16(a)-(c) shows the enlarged ultrasonic echoes from the end and the two notches of UTP at 20°C. As expected, the signal intensity decreases from (a) to (c). During heating periods, the echoes will shift toward higher ToF values due to the elongation of the probe and the decrease in sound velocity inside the wire at higher temperatures. Conversely, the echoes will shift back during the cooling period. However, because of the difference between heating and cooling rate, the evolution of ultrasonic echoes have different behaviors during those periods, as shown in Figs. 16 (d)-(i). The image plots of ToF versus time shown in Figs. 16(d)-(f) display the temporal evolution of the entire echo (peak and sidelobes) within a fixed window from the three locations (notches and the end) along the UTP. For a better presentation of the trend, the evolution of the peak intensity from ultrasonic echoes is plotted out separately in Figs. 16 (g)-(i). The measured temperature with the RTD and the thermocouple probe are shown in Figs. 17 (a) and (b). Comparison of data in Figs 16 and 17 indicates that the measurements made by UTP show the same trend as those made by both RTD and NTC. Based on the sampling rate of the system, the total shift in ToF, and the tested temperature range, the calculated resolution for temperature measurement of our current UTP is estimated to be 0.79 °C.

It is important to note that the resolution for measuring ΔT is limited only by the sampling rate of the current system. While the resolution of current UTP system is considered acceptable for the application at hand, if necessary, it could be further increased to measure smaller ΔT values by employing an acquisition configuration with a higher sampling rate.

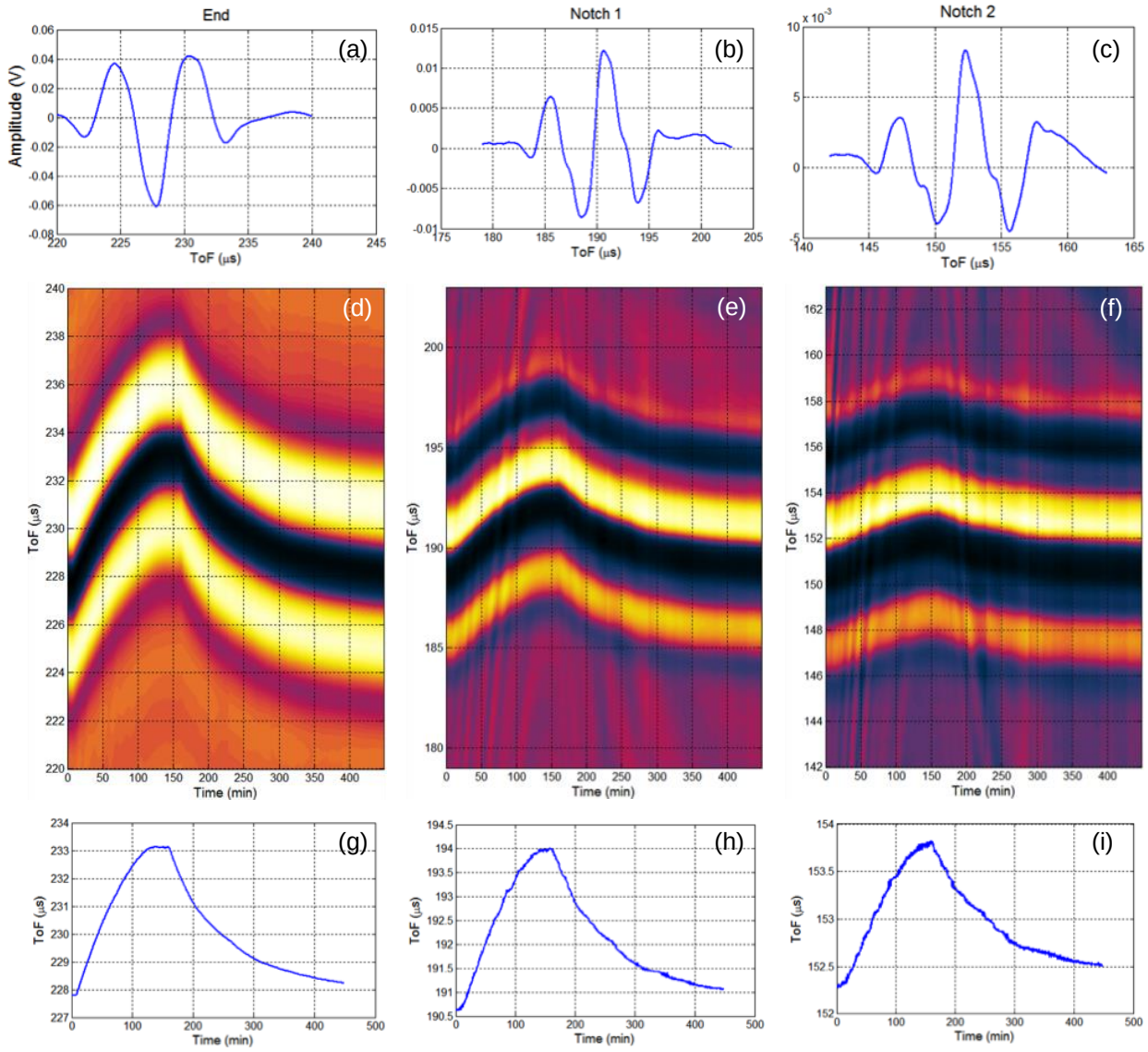

Fig. 16. Data collected with the UTP in straight conformation from 20°C to 400°C. (a)-(c) Ultrasonic echoes from the end and two notches at 20°C; (d)-(f) Evolution of the ultrasonic echoes from the end and two notches during heating (ToF increasing) and cooling (ToF decreasing) period; (g)-(i) Evolution of the peak with maximum intensity of the ultrasonic echoes during heating (ToF increasing) and cooling (ToF decreasing) period.

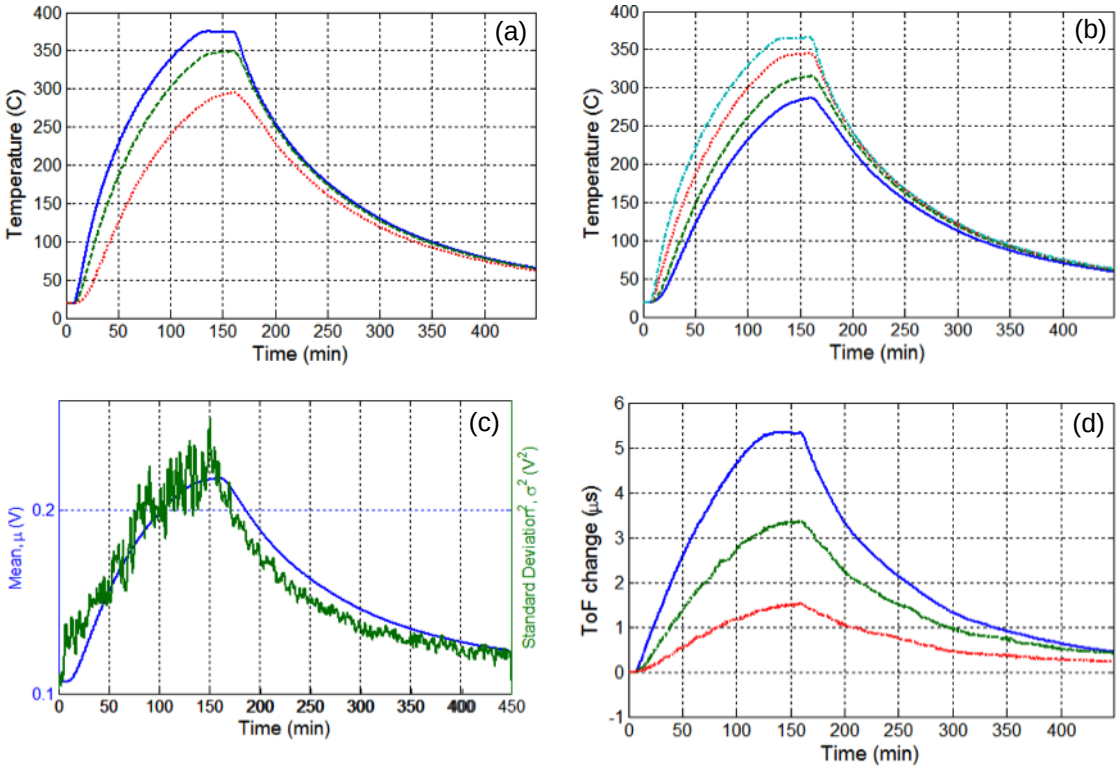

Fig. 17. Data collected as the mockup was heated from 20°C to 400°C with straight UTP conformation. a) RTD data, b) thermocouple data, and c) voltage-derived plots showing RMS value and standard deviation (a measure of Johnson noise), and d) UTP data.

The test results using a straight UTP conformation design with two notches are shown in Fig. 17. Data for those tests was collected while the canister mockup was heated from 20°C to 400°C. The measurements made simultaneously using the RTD and NTC sensors are provided in Figs. 17 (a) and (b), respectively. Both the RTDs and the thermocouples display the same trend with rising temperature. A closer examination of the results indicates that the difference in temperature readings between the same pair of RTD and thermocouple is smaller at lower temperatures (<150 °C) than that at higher temperatures. This deviation could provide important information on comparison of the stability of RTD and NTC probes at elevated temperatures. Investigations are currently under way to better quantify the deviations between those two temperature sensing methods. The measurements of the RMS value of the RTD voltage and the STD value of noise voltage at room temperature (as reference) and at elevated temperatures are given in Fig. 17 (c). The JNT measurement data, which involves multiple stages of signal processing, also closely follows the measured temperature profile recorded with the RTD and the thermocouple probe. Figure 17 (d) is a composite plot of data shown in Fig. 16. Once again, the UTP results for the temperature range in these experiments closely follow the trend seen in the RTD and the NTC data.

In addition to good accuracy, the flexibility of the UTP provides an important advantage over other temperature sensors as the surface-conforming wireline probe allows measurements to be made over complex geometries. This renders the probe particularly suitable for measurement scenarios where access is limited. To demonstrate this capability, the flexible wireline probe was bent and placed diagonally

along the outside surface of the canister mockup, as shown in Fig. 18. The corresponding locations of notches along the contoured probe are also highlighted in that figure. The magnetostrictive transducer (MST) used in the experiment is shown as the inset. To more realistically simulate challenging field scenarios involving confined spaces and limited access, the wireline probe was fed through a small opening at the bottom of the test stand. It is worth noting than in practice, the MST could be placed at much longer distances from the test piece, which helps minimize any potential long-term damage to the sensor's electronics.

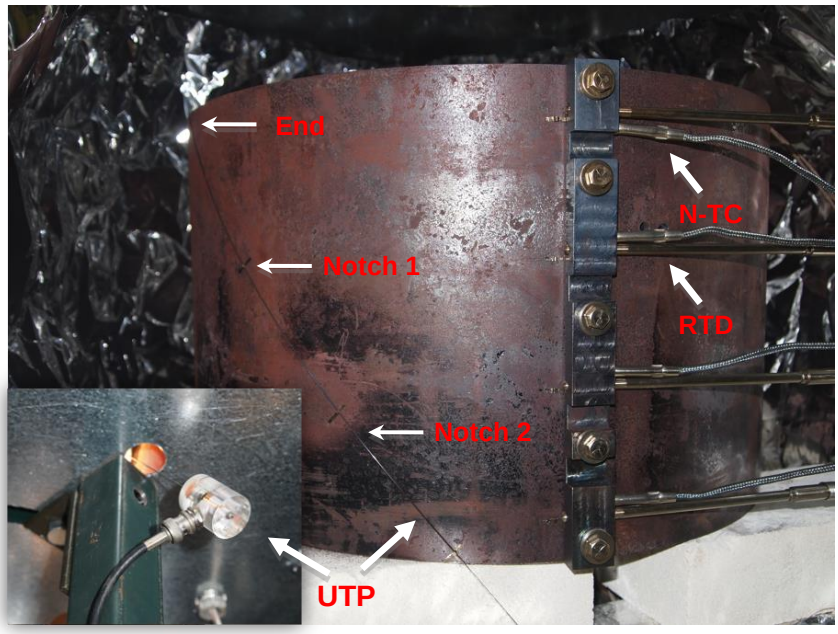

Fig. 18. The approximate position of notches on the UTP in bending conformation setup.

The experimental data collected using the contoured UTP configuration is shown in Fig. 19. The results in general demonstrate that the UTP performs properly even under bending deformation. In this experiment, test conditions were purposely altered during the cooling period to introduce different cooling rates. As highlighted in Fig. 19(g)-(i), the rapid change in cooling rate was clearly picked up by the UTP.

The test results using the bent UTP conformation setup with two notches placed on the wireline sensor are shown in Fig. 20. The data was collected as the mockup was heated from 20°C to 400°C. The measurements from RTDs and NTCs are provided in Figs. 20(a) and (b), respectively. The measurements of the RMS value of the RTD voltage and the STD value of noise voltage at room temperature (as reference) and elevated temperature are given in Fig. 20(c). Figure 20(d) shows the UTP results over the tested range of temperature. The temporal data once again demonstrate that the UTP response closely follows that of RTD and NTC, including at the zone associated with rapid cooling ramp. Based on the results of the investigations conducted so far, the performance of the UTP developed under this work demonstrates the unique advantage of this technology for long-term monitoring of DCSS condition.

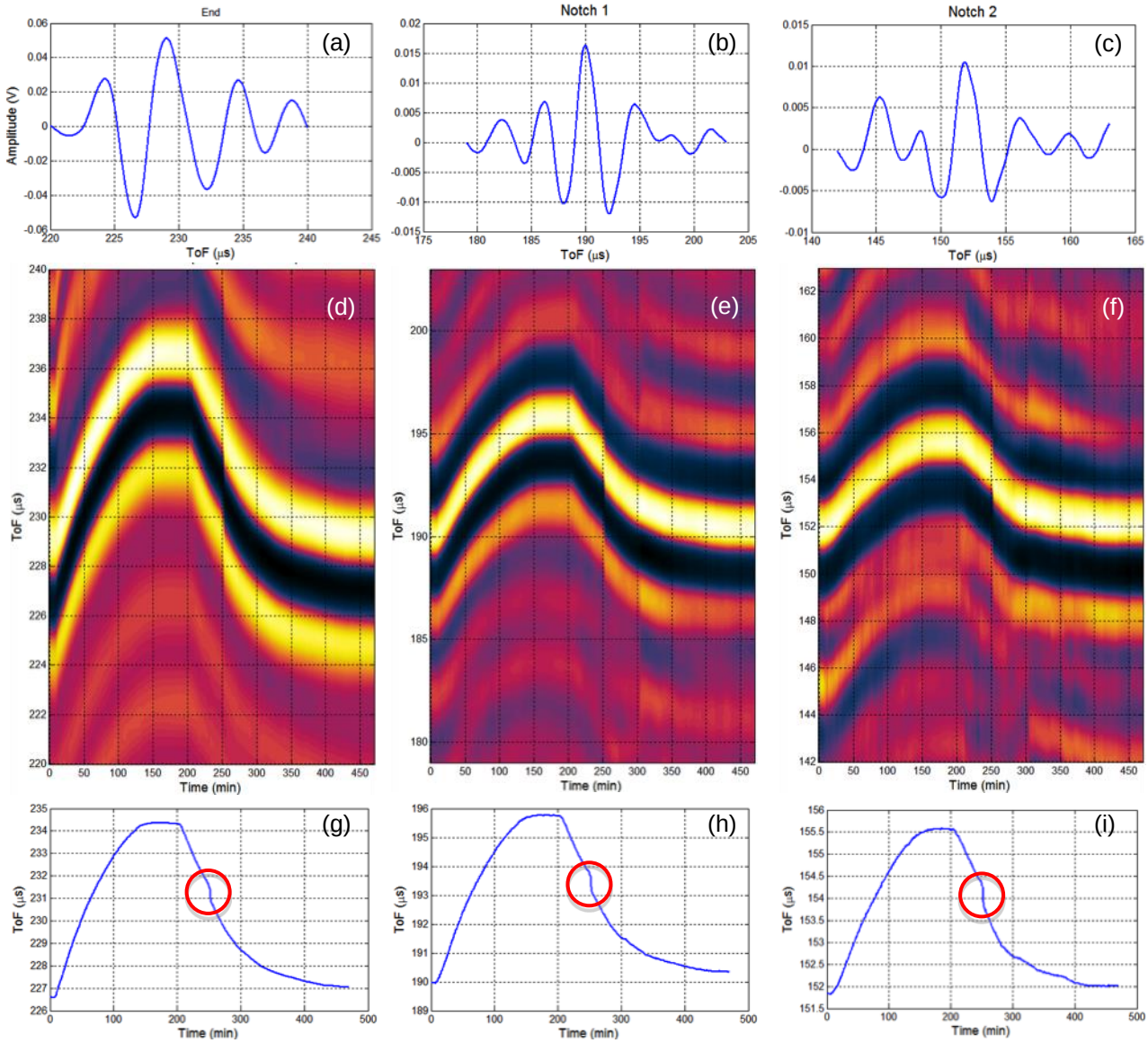

Fig. 19. Data collected with the UTP in bending conformation setup over a temperature of 20°C to 400 °C. (a)-(c) Ultrasonic echoes from the end and two notches at 20°C; (d)-(f) Evolution of the ultrasonic echoes from the end and two notches during heating (ToF increasing) and cooling (ToF decreasing) period; (g)-(i) Evolution of the peak with maximum intensity of the ultrasonic echoes during heating (ToF increasing) and cooling (ToF decreasing) period. The circles mark the location of the rapid change in cooling rate detected by UTP.

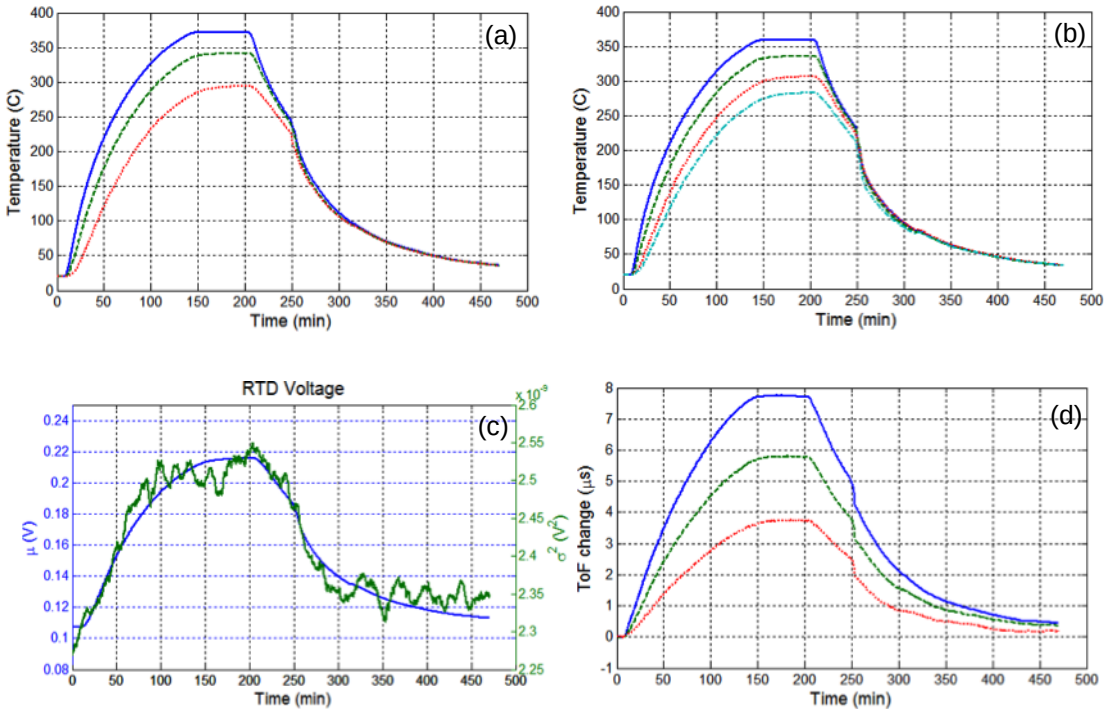

Fig. 20. Data collected with the bent UTP conformation setup as the mockup was heated from 20°C to 400°C. Shown here are a) RTD data, b) Thermocouple data, c) voltage-derived plots showing RMS value and standard deviation (a measure of noise), and d) UTP data.

3.1.5 Passive Millimeter-Wave (mmW) Remote Thermal Imaging

The OLM techniques described earlier all require the sensor to be in contact with the surface of the structure being monitored. The contact-type sensors generally provide a high degree of accuracy and stability. In many practical situations, however, it is preferable to make the measurement in a non-contact manner even when the non-contact method is known to provide a lower degree of accuracy. This is particularly true for situations when measurements are to be made under harsh environmental or accident conditions (e.g., presence of heat, moisture, dust, smoke, and radiation). Furthermore, accessibility of a part and confined spaces could limit the applicability of contact type techniques. Analogous to thermal imaging of objects in the infrared (IR) band, a mmW radiometer can be employed to image the temperature distribution of a structure. As direct consequence of operating at lower energy states (longer wavelength) a mmW radiometer is not expected to provide the degree of sensitivity to surface thermal gradients achievable with a sensitive IR camera. Millimeter-wave radiometry, on the other, offers a number of advantages that make this technology particularly attractive for non-contact monitoring of DCSSs. The main advantages include: (a) all weather capability (i.e., rain, snow, moisture, etc.); (b) day/night operation (i.e., minimally affected by ambient temperature fluctuations); (b) low atmospheric attenuation in comparison to optical/IR techniques; (c) insensitivity to surface condition of the object under interrogation; (d) good depth of penetration into dielectric materials (e.g., common masonry including concrete) allowing subsurface measurement of temperature.

A brief description of the passive mmW sensor (radiometer) developed earlier at ANL is provided below. Representative data collected from an object at elevated temperature with that system is also shown. The system is currently being adapted and evaluated for standoff monitoring of DCSS. Investigations to date have been limited to small-scale laboratory experiments. If successfully demonstrated, this enabling technology could provide a viable alternative sensor for long term monitoring of various DCSS designs and under different environmental conditions.

The experimental setup for the thermal/temperature imaging of objects at elevated temperatures using Argonne's 16-channel radiometer is shown in Fig. 21 (a). A photograph of the system that includes the mmW front-end, focusing optics, back-end electronics, and data acquisition is provided in Fig. 21(b). The radiometer consists of a circular corrugated horn antenna, followed by a 146-154 GHz Band Pass Filter (BPF), a mixing stage, a 164 GHz Local Oscillator (LO) obtained by doubling an 82 GHz Gunn oscillator signal, an attenuator, a three-stage amplifier chain, and a 16-channel filter bank. A chopper is used in front of the scalar horn to collect Dicke-switched data between a reference signal from an absorber on the chopper blades and the target scene viewed through an opening between chopper blades.

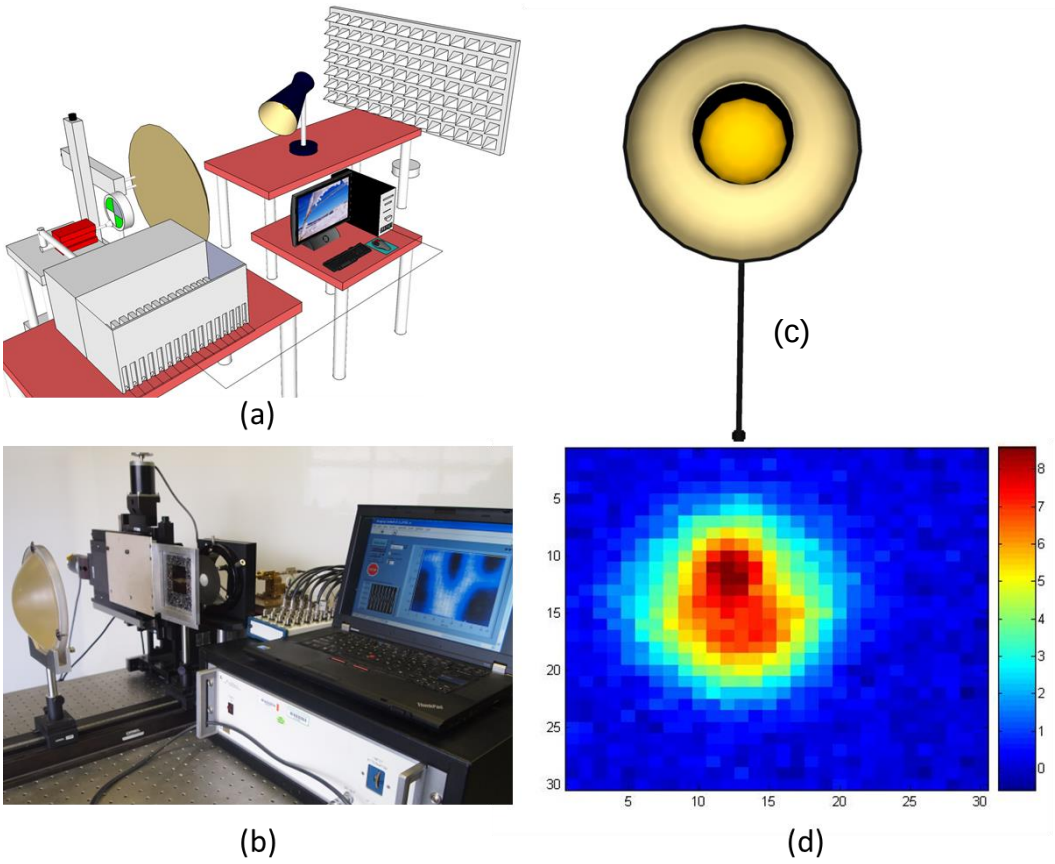

Fig. 21. (a) Experimental setup of mmW radiometer; (b) Photograph of the system; (c) Depiction of heat source under test; and (d) mmW image of the heat source (60W lamp).

The detected signals from 16 channels are collected by a Data Acquisition (DAQ) board interfaced to a Laptop. To obtain 2-Dimensional (2D) images, a 15cm Gaussian lens was raster-scanned against the radiometer antenna positioned at the imaging plane of the lens. The experimental setup of mmW radiometer is shown in Fig. 21. The image result of a 60-Watts desk lamp is shown in Fig. 21(d). It is important to note that similar images can be produced with the mmW sensor even through relatively thick dielectric barriers and ambient conditions. Furthermore, unlike IR cameras which provide only the surface temperature of an object, the mmW sensor provides a measure of effective temperature through the layer thickness. As such, microwave and mmW radiometric techniques could in theory be used to assess the integrity of the shielding material. Studies in this area are currently under way at ANL and the results of investigations will be presented in our future reports.

3.2 In-situ NDE of DCSS Canister

Reliable detection of defects and degradations at welded regions of the metallic canister is a potential concern to long-term structural integrity of DCSS. The presence of residual stresses at dissimilar metal welds, exposure to corrosive environments, and the quality of the workmanship renders the welded regions of the canister prone to a number of manufacturing defects and degradation modes including SCC. Inservice inspection of metal canisters using conventional NDE techniques is a challenging task. The difficulty is associated primarily with the lack of access to the system internals. In a number of DCSS designs a small gap/annulus separates the canister from the external shielding structure (e.g., concrete over-pack). The problem is further exacerbated as the inspection may have to be performed through small openings (air inlet and outlet). Eddy current testing in its various forms is among of the most prominent techniques used for inspection of electrically conducting materials and has been demonstrated to reliably detect surface and near-surface flaws in metallic SSC including DCSS canisters. The confined space of the DCSS, however, limits the use of conventional ECT techniques that commonly require mechanical scanning of a probe over the test piece. High-resolution ECT array probes have been identified as a promising NDE method for in-situ inspection of DCSS canisters. This is because array probe technology allows measurements to be made more efficiently over large areas, thus minimizing the need for elaborate scanning systems.

As one of the tasks under this program, the applicability of ECT array probe technology for in-situ NDE of DCSS canisters is currently being evaluated. Both ANL and INL are involved in this collaborative effort. The work involves,

a. Experimental evaluation of existing ECT array probes
b. Optimization of probe design using numerical electromagnetic modeling
c. Development of modern signal processing and data analysis tools for automatic processing of data

3.2.1 Experimental Evaluations

A series of tests have been conducted to assess the ability of array probes for detection and characterization of flaws in welded regions of the DCSS canister. The experimental efforts so far have been limited to the inspection of calibration samples that resemble the type of welds used for manufacturing of canisters. Figure 22 displays an array probe used at INL to examine the samples. This

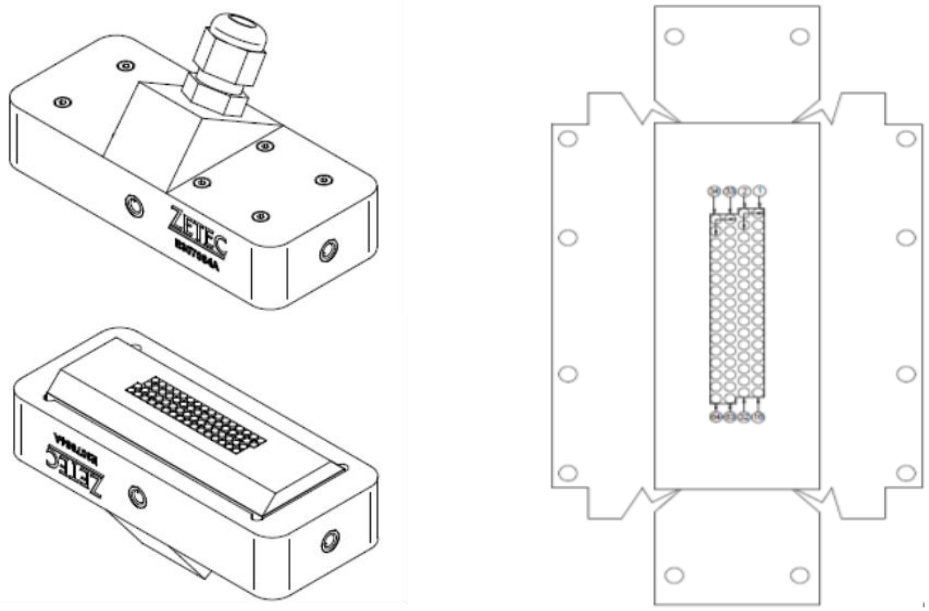

Fig. 22. Array probe with 32 axial and 30 transverse elements. Shown here are the (left) top and bottom view of the probe head and (right) T/R coil configuration.

Source: Sonaspection Int. (Sample PL1436, welds A & B)
Material: SS304, 0.26 in. thick plate (SS308L fill)
Weld Process: GTAW

Defect Number	Crack Length (in.)	Crack Depth (in.)
1	0.232	0.125
2	0.377	0.125
3	0.108	0.125
4	0.420	0.125

(a)

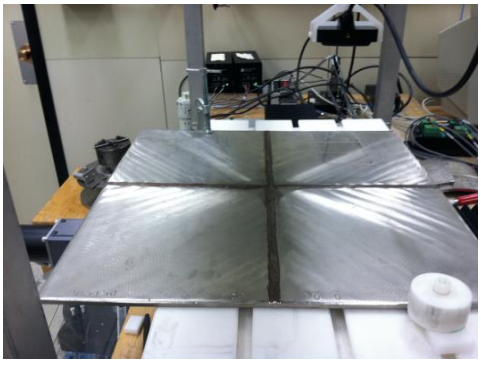

(b)

Fig. 23. (a) Sonaspection plate with transverse weld cracks and tabulated data providing a list of flaws present in the sample, and (b) typical scanning setup for inspection of samples.

probe head houses 32 axial and 30 transverse probes. The probes operate in driver-pickup/transmit-receive (T-R) mode and may be excited at a wide range of frequencies. The surface conforming design ofthe array probe allows scanning of contoured surfaces while minimizing the probe lift-off effects. The samples were all scanned with the probe mounted on a computer controlled two-axis translation stage. All data acquisition at INL was performed using a commercially available eddy current instrument and the associated software. Figure 23(a) displays a representative calibration standard sample with manufactured flaws that were used in the initial phase of our evaluations. Also provided in that figure is the listing of manufactured flaws included in the sample. The scanning setup is depicted in Fig. 23(b).

Eddy current inspection data collected at INL from a sample with manufactured flaws indentified as "3-toe cracks" is shown in Fig. 24(a). The image display, strip-chart and impedance plots over a small region of the sample using the commercial software are shown in the main analysis window. To allow off-line processing of data using the data analysis tool developed at ANL, a series of routines were implemented to convert, calibrate, and import the data for subsequent analysis. The ANL data analysis tool is made up of various algorithms developed under the MATLAB® environment for visualization, measurement, calibration, signal processing and analysis of eddy current inspection data. The algorithms are all linked under a common graphical user interface (GUI). Figure 24(b) displays the same data as Fig. 24(a) in image and stipchart format. The location of flaws in the processed data are marked both on vertical component of the c-scan image and along the strip-chart plot. In comparison to Fig. 24(a), the results in Fig. 24(b) clearly indicate significant improvement in signal-to-noise ratio (S/N) following the application of the signal processing routines available under ANL data analysis tool. The signal here refers to the probe response from cracks and the noise refers to all other unwanted indications including the probe response to the large discontinuity associated with the weld zone.

Another example on improving detection of flaws using modern signal processing and data analysis algorithms is shown in Fig. 25. Various stages of data analysis performed on the same data at ANL are shown in Fig. 25(a)-(c). Once again the processed data shows significant improvement in detection of the three flaws included in the weld sample. In reference to Fig. 25, there is a clear improvement in S/N at each subsequent stage of processing resulting in near total elimination of the large interfering signal from the weld. The results of investigations so far suggest that the eddy current data analysis tool developed at ANL could be used to automate detection, identification and sizing of flaws in DCSS canister welds.

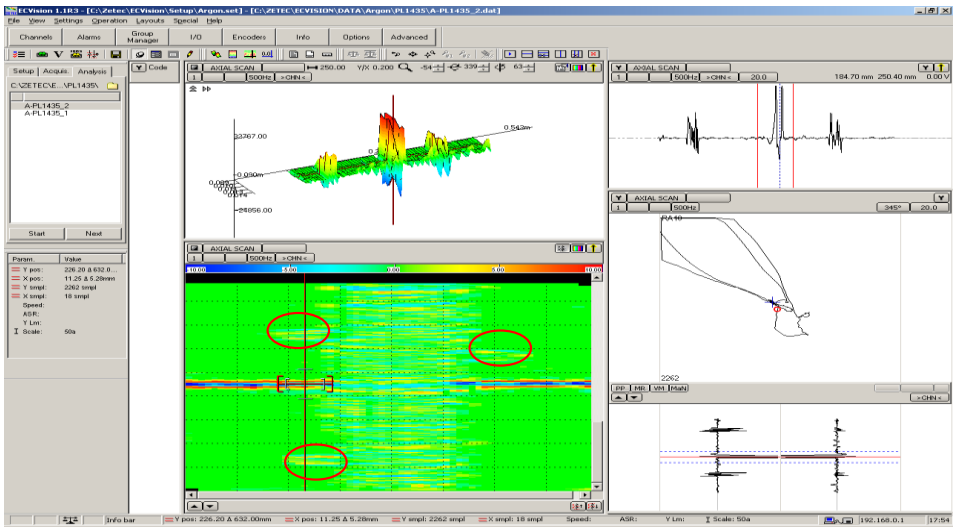

(a)

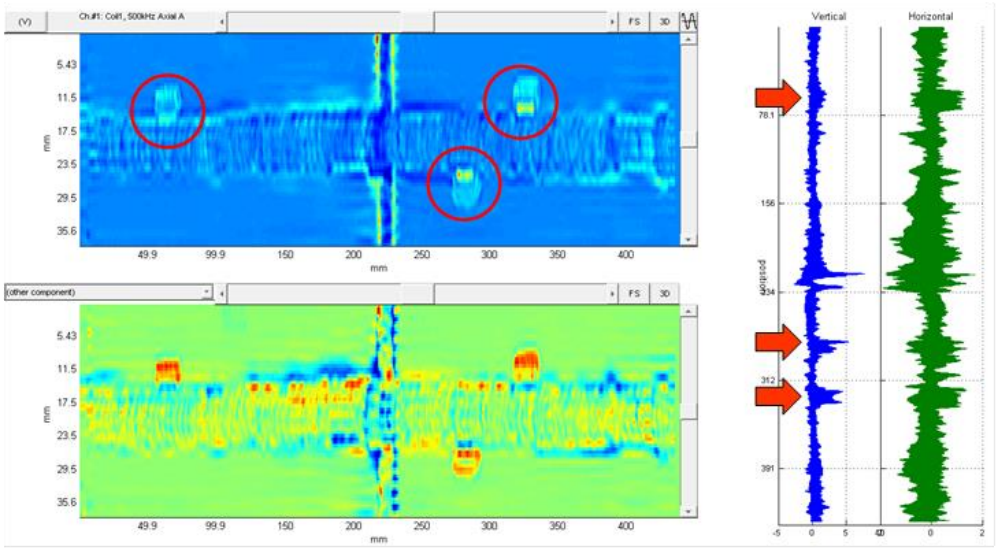

(b)

Fig. 24. Eddy current inspection data collected at INL from Sonaspection plate containing “3-toe cracks”. Shown here are (a) data displayed over a small section of the sample using the commercial software and (b) processed data using the ANL data analysis software with the location of flaws marked by circles and arrows.

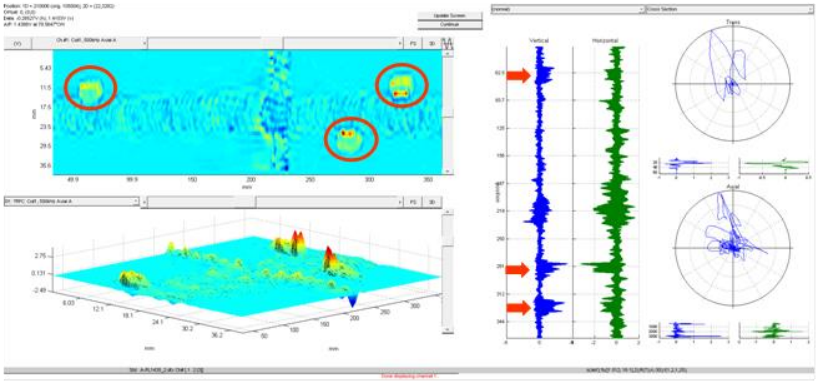

(a)

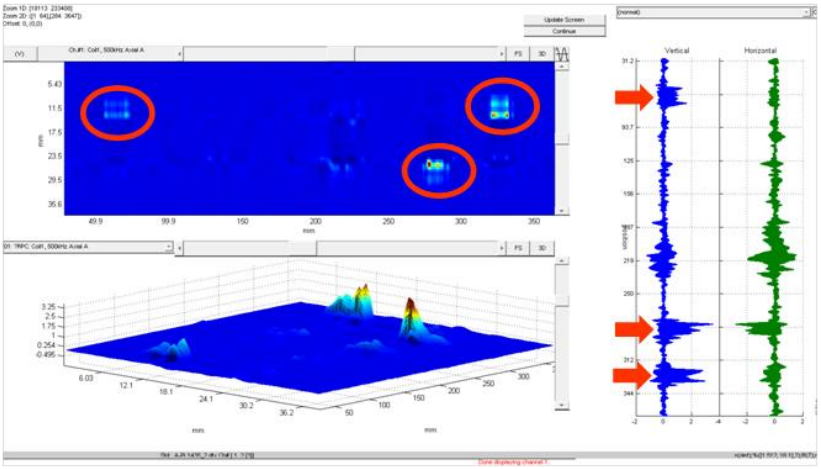

(b)

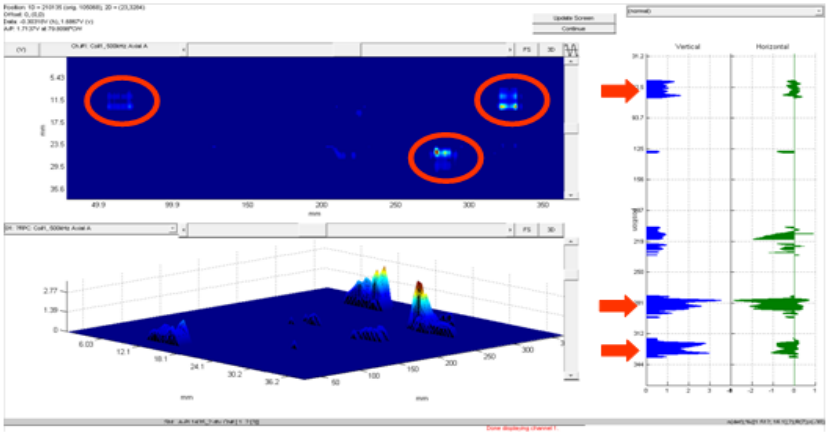

(c)

Fig. 25. Eddy current inspection data collected at INL from Sonaspection plate containing “3-toe cracks” shown in Fig. 24(a). Displayed here are data at various stages of processing using the ANL data analysis software with the location of flaws marked by circles and arrows.

3.2.2 Numerical Electromagnetic Modeling

Numerical simulations were also conducted to help optimize the design of T-R array probe. As noted earlier, the purpose of this study was to increase the probe coverage with the same number of elements (practical manufacturing constraint) while maintaining acceptable sensitivity to detection of limiting flaws. A hybrid 3-D numerical electromagnetic code based on volume integral formulation was used for modeling of the eddy current probe response. Representative test cases on the variation of complex impedance as a function of changes in coil position, flaw depth, T-R coil spacing, and coil size are presented next. For the test cases shown here the test piece was modeled as a flat plate of type 304 SS material with conductivity of $\sigma = 1.45 \times 10^6$ (S/m), relative permeability of $\mu_r = 1$, and with a thickness represented by an infinite half-space. The latter assumption is valid in view of typical DCSS canister wall thickness, T, and the operating frequency ($T >> 3\delta$, where δ is the eddy current skin depth). Unless specified otherwise, the flaw is an outer-diameter surface-breaking crack with a length of L = 12 mm (~0.5 in.), a depth of d = 1 mm, and a width (opening) of w = 0.05 mm. Although the effect of frequency was has been evaluated separately, for all the calculations here an excitation frequency of f = 100 kHz was used as the default value. The nominal coil dimensions for both the transmitter and the receiver element are: inner diameter = 0.5 mm, outer diameter = 2.0 mm, height = 0.25 mm, and coil spacing = 0.5 mm (i.e., center-to-center spacing of 2.5 mm). The coils were arbitrarily chosen to be made of 100 turns of copper wire.

A series of test were initially conducted to validate the numerical results. Figure 26 shows the probe response to the default crack for different probe positions. The scans represent probe motion along the coil axis and transverse to the flaw axis. To simulate typical calibrated measurements, in all cases the phase angle of the coil impedance was rotated such that the lift-off signal is nearly horizontal. Figure 26(a) shows the impedance plot for a series of transverse scans at different locations along the flaw axis. The middle of the crack is at 0 mm and the end of the crack (L/2) is at 6 mm. Figure 26(b) shows the magnitude plot of the impedance values, |Z|, shown in Fig. 26(a) as a function of position in transverse direction. As expected, the signal amplitude drops as the probe moves toward the edge and eventually away from the crack. The composite terrain plots generated from raster scan values for the vertical and horizontal components of the impedance are shown in Fig. 26(c).

Calculated probe response for various crack depths between 0.25 mm and 3 mm are shown in Fig. 27. Once again, impedance plane trajectories for five transverse scans to flaw axis along the line crossing the middle of the crack are shown in Fig. 27(a). The magnitude plots (|Z|) as a function of probe position along the scan direction for the same data as Fig. 27(a) are shown in Fig. 27(b). The results show roughly an order of magnitude change between the deepest and shallowest flaw. The calculated values also indicate the ability of the probe to detect even the shallowest flaw modeled here.

The simulated eddy current T-R probe response to a 12-mm long surface breaking crack in for three different coil spacing (gap) of 0.5 mm, 1 mm, and to 2 mm are shown in Fig. 28. The impedance plane trajectories for transverse scans to flaw axis along the line crossing the middle of the crack are shown in Fig. 28(a). The magnitude plots (|Z|) along the scan direction as a function of position are shown in Fig. 28(b). In this particular case, the results generally display a drop by approximately a factor of 5 due to four fold increase in the nominal coil-to-coil spacing. Calculated impedance values for different coil diameters, ranging from 1.5 mm (nominal value) to 4 mm, are shown in Fig. 29. The results in this case indicate that increasing the coil diameter up to a certain size (~3 mm) can improve the

detection sensitivity. Larger coil diameters beyond the optimum value on the other hand will lead to degradation in sensitivity in conjunction with reduced spatial resolution. This is expected as the volume fraction of the flaw within the coil field of view will be reduced for larger coil dimensions. In view of the data shown in Figs. 28 and 29, the results of numerical simulations suggest that using the same number of elements the array probe coverage could be increased through a combination of increased coil diameter and coil spacing with the optimized design parameters dictated by the eddy current test parameters (i.e., material properties and dimensions and minimum expected flaw size which also dictates the operating frequency). More extensive numerical simulations, however, must be conducted to determine the optimum probe design parameters to ensure acceptable detection sensitivity and spatial resolution for the wide range of test conditions that could be encountered during field examinations.

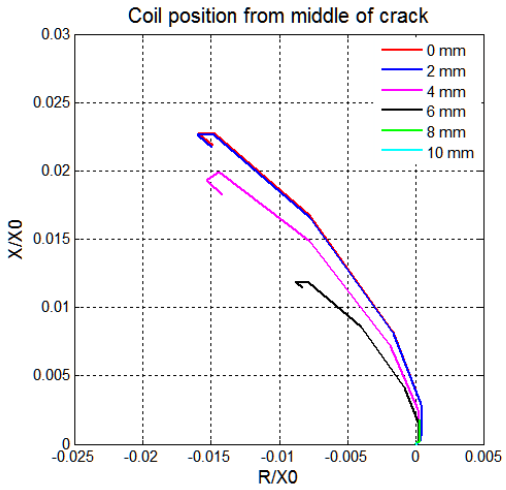

(a)

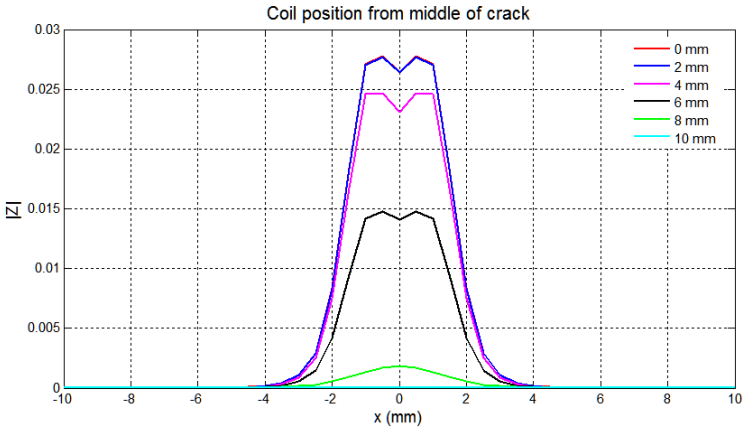

(b)

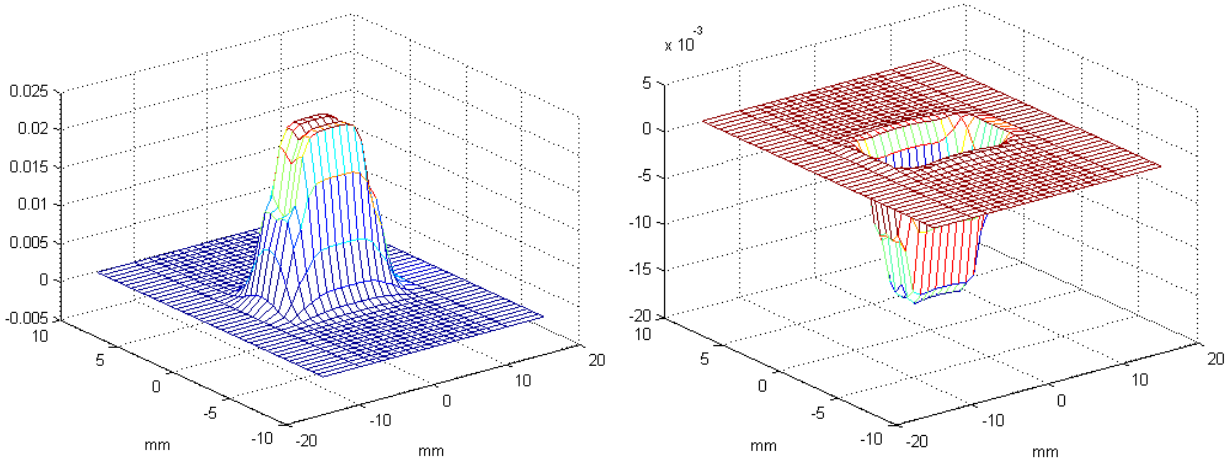

Vertical component Horizontal component

(c)

Fig. 26. Simulated eddy current T-R probe response to a 12-mm long, 1-mm deep surface breaking crack in a type 304 SS plate as a function of probe position. Shown here are (a) impedance plane trajectories for six transverse scans to flaw axis (middle of crack at 0 mm), (b) magnitude plot (|Z|) along transverse direction, and (c) terrain plots generated from raster scan data.

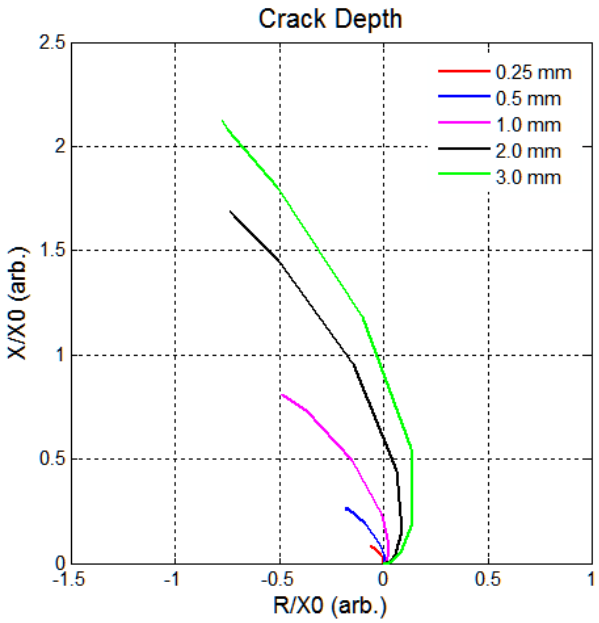

(a)

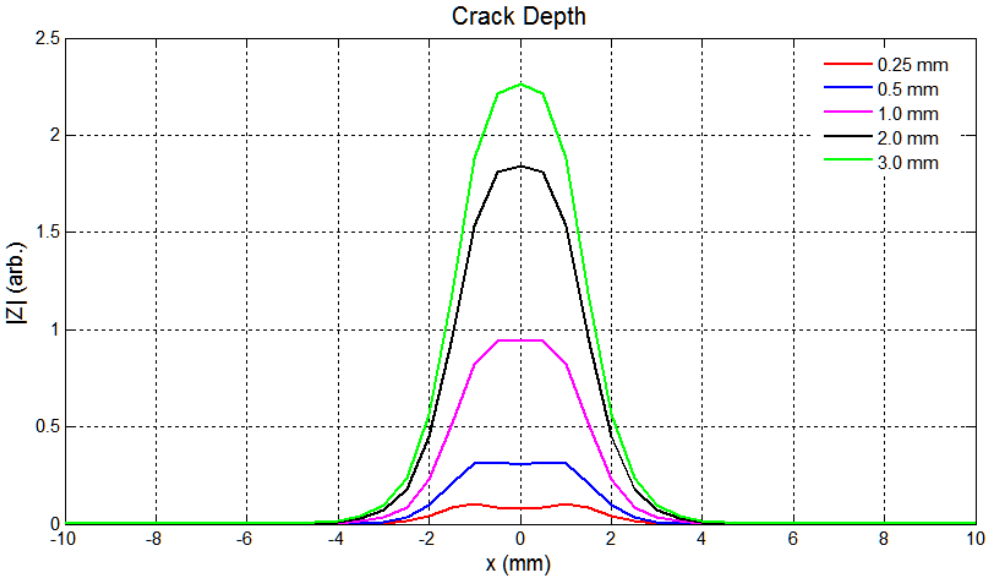

(b)

Fig. 27. Simulated eddy current T-R probe response to a 12-mm long surface breaking cracks ranging from 0.25 mm to 3 mm deep in a type 304 SS plate. Shown here are (a) impedance plane trajectories for five transverse scans to flaw axis along the line crossing the middle of the crack and (b) magnitude plot (|Z|) along transverse direction as a function of position.

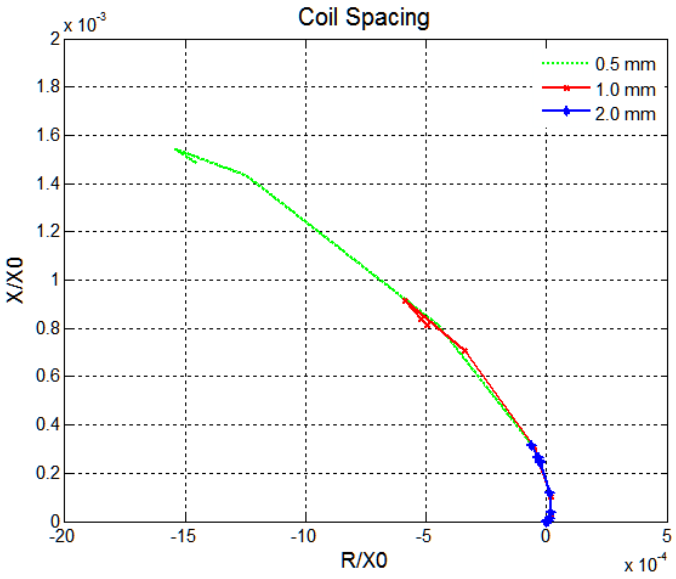

(a)

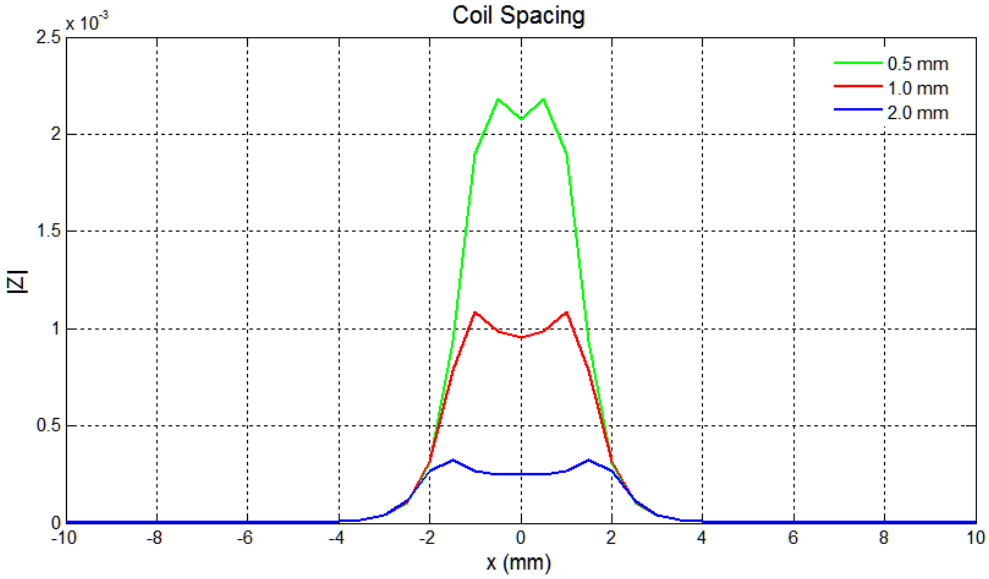

(b)

Fig. 28. Simulated eddy current T-R probe response to a 12-mm long surface breaking crack in a type 304 SS plate for three different coil spacing/gaps ranging from 0.5 mm to 2 mm. Shown here are (a) impedance plane trajectories for transverse scans to flaw axis along the line crossing the middle of the crack and (b) magnitude plot (|Z|) along transverse direction as a function of position.

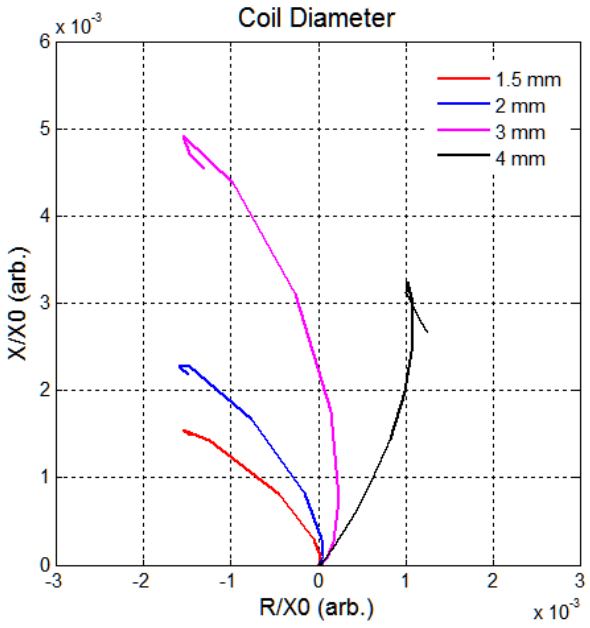

(a)

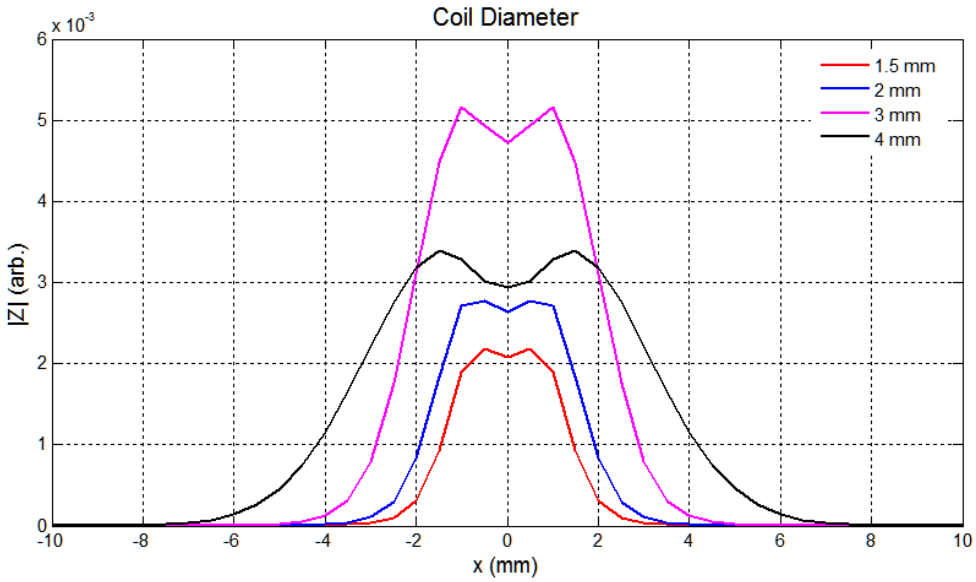

(b)

Fig. 29. Simulated eddy current T-R probe response to a 12-mm long surface breaking crack in a type 304 SS plate for four different coil diameters ranging from 1.5 mm to 4 mm. Shown here are (a) impedance plane trajectories for transverse scans to flaw axis along the line crossing the middle of the crack and (b) magnitude plot (|Z|) along transverse direction as a function of position.

4. Future Plans

Efforts are expected to continue on further evaluation of promising OLM and in-situ NDE techniques for DCSSs that were discussed in this report. Initial results of investigations to date suggest that JNT and UTP technique are well suited for long term monitoring of DCSSs. Further investigations, however, are needed to demonstrate the applicability of those two emerging technologies for the application at hand. Future work in this area will include (a) sensitivity analyses to quantify potential improvements over conventional measurement methods, (b) long-term performance of the sensors under large temperature cycling and step ramping, (c) viable mechanical fixtures for sensor attachment–permanent or detachable, (d) packaging of the sensors for field application, and (e) testing of selected sensor technologies at a designated facility. Future plans on the evaluation of OLM techniques include demonstration of the applicability of mmW radiometry for non-contact imaging of DCSS temperature distribution. Parallel efforts will also continue on the evaluation of eddy current array probe technology for rapid inspection of DCSS canisters. The focus of the investigations will once again be on reliable detection and characterization of flaws at welded regions. To that end, numerical modeling will be performed to optimize the probe design. The aim in this case is to increase the probe coverage using the minimum number of T-R elements while maintaining the sensitivity to detection of limiting flaws. Efforts will also continue on adaptation of the signal processing and data analysis algorithms to the processing of data collected from representative samples. The ultimate goal is to fully automate the detection and characterization of flaws for field applications.

5. Glossary

Resistance Temperature Device, RTD

An accurate, stable thermometer based upon a coil of pure, metal wire of known, stable resistivity. In this case, the RTD is a general purpose, class A device fabricated from a coil a platinum wire having a resistance of 100.00 ±0.06 ohms at the triple point of water, 273.15ºK (0.0ºC) and exhibits a linear resistance change of 0.00385 ohms/ohm/ºC. It is contained in an Inconel 600 sheath and useable to 600ºC.

Virtual Instrument, VI

A VI is a Labview Virtual Instrument comprised of a software program based upon G-code whose appearance and operation imitate physical instruments.

Multithreading

LabVIEW automatically divides each application into multiple execution threads. Multithreading extends the idea of multitasking into applications, so you can subdivide specific operations within a single application into individual threads. Each of the threads can run in parallel. The OS divides processing time not only among different applications, but also among each thread within an application. Thus, in multithreaded applications, multiple tasks can progress in parallel with other applications that are running on the system. [http://zone.ni.com/devzone/cda/tut/p/id/6424]

Notifier

Notifier Operations functions suspend the execution of a block diagram until you receive data from another section of the block diagram or from another VI running in the same application instance. Unlike the Queue Operations functions, the Notifier Operations functions do not buffer sent messages. If no nodes are waiting on a message when it is sent, the data is lost if another message is sent. Notifiers behave like single-element, bounded, lossy queues. [http://zone.ni.com/reference/en-XX/help/371361E-01/glang/notification_vis/]

Queue

Queue Operations functions create a queue for communicating data between sections of a block diagram or from another VI. [http://zone.ni.com/reference/en-XX/help/371361E-01/glang/queue_vis/]

Rendezvous

Rendezvous VIs synchronize two or more separate, parallel tasks at specific points of execution. Each task that reaches the rendezvous waits until the specified number of tasks are waiting, at which point all tasks proceed with execution. [http://zone.ni.com/reference/en-XX/help/371361E-01/glang/rendezvous_vis/]

TDMS file

National Instruments introduced the Technical Data Management Streaming (TDMS) file format as a result of the deficiencies of other data storage options commonly used in test and measurement applications. The binary TDMS file format is an easily exchangeable, inherently structured, high-speed-

streaming-capable file format that, becomes quickly searchable without the need for complicated database design, architecture, or maintenance.

[For NI TDMS file format see: http://zone.ni.com/devzone/cda/tut/p/id/3727]

Nicrosil/Nisil (Type N) Thermocouples

The type N thermocouple is based upon Nicrosil/Nisil alloys that offer better stability than existing base-metal type E, J, K and T thermocouples. ANSI standard base-metal type E, J, K and T thermocouples show inherent thermoelectric instability related to time and/or temperature dependent instabilities in several of their physical, chemical, nuclear, structural and electronic properties.

There are three principal characteristics and types of thermoelectric instability in the standard, base-metal materials:

1. A gradual and generally cumulative drift in thermal electromotive force (EMF) occurs when exposed to elevated temperatures for extended time periods. This is due to changes in composition caused mainly by internal oxidation. Further, neutron radiation produces transmutation of some of the constituents in nuclear environments.
2. A short-term, cyclic change in thermal EMF occurs with E, J, K and T types when heated to 250ºC - 650ºC. It is suspected this is due to a structural change, such as magnetic short-range order.
3. A time-independent perturbation in thermal EMF occurs within specific temperature ranges due to composition dependent magnetic transformations. For type K this range is 25 – 225ºC and for type J it is above 730ºC.

Nicrosil/Nisil thermocouples have shown very high thermoelectric stability via judicious choice of elemental materials. Nicrosil has increased concentrations of silicon and chromium added to a pure nickel base that minimizes or eliminates oxidation effects. Thermal EMF instabilities have been virtually eliminated by increasing the weight-percent of chromium. Silicon and magnesium in Nisil oxidize preferentially forming oxidation resistant films. Furthermore, magnetic transformations are suppressed by the elevated weight-percent of silicon and relative freedom from nuclear transmutation has been achieved by eliminating manganese, cobalt and iron. [Burley, Noel A., "Nicrosil/Nisil Type N Thermocoouples", http://www.omega.com/pdf/temperature/Z/pdf/z041-044.pdf]

Nuclear Engineering Division
Argonne National Laboratory
9700 South Cass Avenue, Bldg. 308
Argonne, IL 60439

www.anl.gov